

Redshift-Space Distortions with the Halo Occupation Distribution II: Analytic Model

Jeremy L. Tinker^{1*}

¹*Kavli Institute for Cosmological Physics, University of Chicago, 933 E. 56th St., Chicago, IL 60637*

ABSTRACT

We present an analytic model for the galaxy two-point correlation function in redshift space. The cosmological parameters of the model are the matter density Ω_m , power spectrum normalization σ_8 , and velocity bias of galaxies α_v , circumventing the linear theory distortion parameter β and eliminating nuisance parameters for non-linearities. The model is constructed within the framework of the Halo Occupation Distribution (HOD), which quantifies galaxy bias on linear and non-linear scales. We model one-halo pairwise velocities by assuming that satellite galaxy velocities follow a Gaussian distribution with dispersion proportional to the virial dispersion of the host halo. Two-halo velocity statistics are a combination of virial motions and host halo motions. The velocity distribution function (DF) of halo pairs is a complex function with skewness and kurtosis that vary substantially with scale. Using a series of collisionless N-body simulations, we demonstrate that the shape of the velocity DF is determined primarily by the distribution of local densities around a halo pair, and at fixed density the velocity DF is close to Gaussian and nearly independent of halo mass. We calibrate a model for the conditional probability function of densities around halo pairs on these simulations. With this model, the full shape of the halo velocity DF can be accurately calculated as a function of halo mass, radial separation, angle, and cosmology. The HOD approach to redshift-space distortions utilizes clustering data from linear to non-linear scales to break the standard degeneracies inherent in previous models of redshift-space clustering. The parameters of the occupation function are well constrained by real-space clustering alone, separating constraints on bias and cosmology. We demonstrate the ability of the model to separately constrain Ω_m , σ_8 , and α_v in models that are constructed to have the same value of β at large scales as well as the same finger of god distortions at small scales.

Key words: cosmology: theory — galaxies: clustering — large-scale structure of universe

1 INTRODUCTION

The growth of structure through gravity creates peculiar velocities with respect to the smooth Hubble flow, making the line of sight a preferred direction when redshift is used as a measure of distance. The systematic differences between the distribution of structure in real and redshift space contain information about both the cosmology of the universe and the bias of galaxies observed (see, e.g., Peebles 1976; Sargent & Turner 1977; Kaiser 1987). In Pa-

per I (Tinker et al. 2006a), we used numerical simulations to develop a blueprint for determining cosmological parameters from redshift-space distortions. In this paper, we use those simulations to calibrate an analytic model for redshift-space galaxy clustering that has the necessary accuracy to interpret high-precision measurements from large-scale galaxy redshift surveys, like the Two-Degree Field Galaxy Redshift Survey (2dFGRS; Colless et al. 2001) and the Sloan Digital Sky Survey (SDSS; York et al. 2000).

The effect of redshift-space distortions is most apparent at small scales, where the internal motions of galaxies in groups and clusters spread out close pairs along the line of

* E-mail: tinker@cfcf.uchicago.edu

sight, creating the so-called “fingers-of-god” (FOGs). This picture of clustering in redshift space can be expressed as a convolution of the real-space two-point correlation function $\xi_R(r)$ with the probability distribution function (PDF) of galaxy pairwise velocities $P(v_z)$, i.e.,

$$1 + \xi(r_\sigma, r_\pi) = \int_{-\infty}^{\infty} [1 + \xi_R(r)] P(v_z) dv_z, \quad (1)$$

where $\xi_R(r)$ is the real-space correlation function, r_σ is the projected separation, r_π is the line-of-sight separation, $r^2 = r_\sigma^2 + z^2$, and $v_z = H(r_\pi - z)$, where H is the Hubble constant. Equation (1) is often referred to as the “streaming model” (Peebles 1980). Although this approach has been used primarily to model observations of small-scale distortions (e.g., Peebles 1979; Davis & Peebles 1983; Bean et al. 1983), equation (1) is valid in the linear regime as well (Fisher 1995). Scoccimarro (2004) demonstrated that, provided $P(v_z)$ is correct, the streaming “model” is a valid description of the relation between the real- and redshift-space correlation functions on all scales.

As presented, equation (1) contains no cosmology. The aforementioned investigations utilized the streaming model to estimate the velocity dispersion of galaxy pairs, which was used to estimate the matter density parameter Ω_m through a “cosmic virial theorem”. More recent studies of redshift-space distortions have utilized a modified linear theory model of anisotropies that, when applied to the real-space galaxy power spectrum $P_R(k)$, takes the form

$$P_Z(k, \mu) = P_R(k)(1 + \beta\mu^2)^2(1 + k^2\sigma_k^2\mu^2/2)^{-1}, \quad (2)$$

where $\beta = \Omega_m^{0.6}/b_g$, b_g is the linear bias parameter, and μ is the cosine of the angle between the wavevector k and the line of sight. The term $(1 + \beta\mu^2)^2$, derived from linear theory by Kaiser (1987), models the coherent flow of matter out of underdense regions and into overdense regions. The last term on the right hand side represents an exponential distribution of random, uncorrelated peculiar velocities, which dominates P_Z on small scales and is meant to encapsulate the FOG effect described above. Equation (2), commonly referred to as the “dispersion model”, has two free parameters, β and the galaxy velocity dispersion σ_k . Scoccimarro (2004) points out several deficiencies in this model, both in the inability of linear theory to properly describe anisotropies even in the large-scale limit, and in the oversimplification of using a single parameter σ_k , which has no clear physical definition, to model small-scale velocities. Consequently, equation (2) introduces a 10 – 15% systematic error in the determination of β (Hatton & Cole 1999; Paper I), a level of error significant compared with the precision achievable with SDSS and the 2dFGRS.

The goal of this paper is to create an analytic model for the redshift-space correlation function by combining the streaming model of equation (1) with the Halo Occupation Distribution (HOD; see, e.g., Jing et al. 1998; Ma & Fry 2000; Peacock & Smith 2000; Seljak 2000; Benson 2001; Scoccimarro et al. 2001; Berlind & Weinberg 2002; Cooray & Sheth 2002). The HOD quantifies bias on both linear and non-linear scales for a given galaxy sample by specifying the probability $P(N|M)$ that a halo of mass M

contains N galaxies of a given type, together with any spatial and velocity biases between galaxies and dark matter within individual halos. The HOD has been utilized to model the real-space clustering of galaxies in the SDSS (Zehavi et al. 2004, 2005; Tinker et al. 2005) and the 2dFGRS (Tinker et al. 2006b; see also Yang et al. 2003). In this paper we extend the HOD model from real space to redshift space by providing a model for $P(v_z)$ which is physically motivated and empirically calibrated on numerical simulations.

Several recent papers have presented calculations of redshift-space distortions using halo models of dark matter and galaxy clustering (Seljak 2001; White 2001; Kang et al. 2002; Cooray 2004; Skibba et al. 2005; Slosar et al. 2006), providing insight into the role of non-linear dynamics and non-linear bias in shaping clustering and anisotropy. However, these studies rely on the same linear theory component of equation (2) for large-scale anisotropies. Kang et al. (2002) show that their model only reproduces the dark matter $P_Z(k, \mu)$ from N-body simulations after introducing a σ_k parameter for the *halos*, even after the virial motions of particles within halos were taken into account. Skibba et al. (2005) demonstrate the difficulty is modeling redshift-space galaxy clustering in the transition region between quasi-linear and fully non-linear regimes using a linear theory description of halo velocities. Other recent papers have used the halo approach to model galaxy and dark matter velocity statistics (Sheth et al. 2001a; Sheth & Diaferio 2001; Sheth et al. 2001b). While the model outlined in these papers is derived from first principles, in contrast to the calibrated model presented here, it is still based on linear theory, which does not provide the required accuracy for a robust implementation of equation (1). The purpose of our model is less as a first-principles derivation of $P(v_z)$ than as a tool to extract information from forthcoming observational data. In this context, the accuracy of the model is the paramount concern. In the course of developing the model, we will also gain new insight into the physics that determines $P(v_z)$, especially the role of environment in producing a non-Gaussian velocity distribution.

An accurate model for $\xi(r_\sigma, r_\pi)$ with the HOD must properly incorporate halo motions. A proper model for halo pairwise velocities $P_h(v)$ must correctly describe the distribution function for an arbitrary pair of halo masses, at any angle with respect to the line of sight, and as a function of separation. In the large-scale limit, linear theory is adequate for describing the mean infall velocities of halos (see, e.g., Juszkiewicz et al. 1999; Sheth et al. 2001a). However, the applicability of linear theory is problematic at scales where the observational data are robust. At all scales, linear theory does not accurately predict the pairwise dispersion (Scoccimarro 2004). Higher order moments also play an important role in $P_h(v)$. N-body results have shown that the radial velocity PDF of dark matter halos exhibits significant skewness and kurtosis (Zurek et al. 1994; Juszkiewicz et al. 1998).¹ The skewness arises from the infall of matter into overdense regions (Juszkiewicz et al. 1998). The kurtosis,

¹ In this paper we use the convention of *radial* being the direction

manifesting as exponential wings in both the radial and tangential velocities, is due to local non-linear effects for each halo in the pair. Scoccimarro (2004) concludes that a Gaussian is *never* a good description of velocities, even at the largest scales. Scoccimarro (2004) focuses on velocity statistics of dark matter, but local non-linear effects apply to halos as well (Kang et al. 2002), and $P_h(v)$ from simulations are non-Gaussian at all scales. It is not sufficient for $P_h(v)$ to describe the first two moments of the velocity distribution. To accurately model $\xi(r_\sigma, r_\pi)$, $P_h(v)$ must reasonably describe higher order moments of the distribution as well (see, e.g., Fisher et al. 1994).

As stated in Paper I, our method for analyzing redshift-space distortions is to first use measurements of the projected correlation function $w_p(r_p)$ to determine the parameters of the HOD for a given cosmology. If HOD parameters cannot be found that allow the cosmological model to reproduce the observed $w_p(r_p)$ then that model is ruled out. Once the HOD has been determined, the redshift-space clustering is investigated by the analytic model presented here or the N-body approach of Paper I. The cosmological parameters that most directly influence redshift-space clustering are the matter density parameter Ω_m , the amplitude of the linear matter power spectrum, defined here by σ_8 , the rms linear-theory mass fluctuation in $8 h^{-1}\text{Mpc}$ spheres (where $h \equiv H_0/100 \text{ km s}^{-1} \text{ Mpc}^{-1}$), and the velocity bias of the galaxy sample, which we parameterize by α_v , the ratio between the satellite galaxy velocity dispersion and the virial velocity dispersion of the dark matter halo. One can consider models in which the velocities of central galaxies are biased with respect to mean motion of the host halo. In Paper I we considered the shape of the linear matter power spectrum $P_{\text{lin}}(k)$ to be determined by measurements of the cosmic microwave background (CMB) anisotropies and the large-scale galaxy power spectrum (e.g., Percival et al. 2002; Spergel et al. 2003; Tegmark et al. 2004a). An advantage of the analytic model for $\xi(r_\sigma, r_\pi)$ is that it allows for marginalization over $P_{\text{lin}}(k)$ without the cumbersome process of running multiple N-body simulations. The redshift-space observables explored here and in Paper I are largely independent of $P_{\text{lin}}(k)$, thus the constraints on HOD parameters come primarily from $w_p(r_p)$ and to a small degree the assumed $P_{\text{lin}}(k)$, and the constraints on our cosmological parameter space of Ω_m , σ_8 , and α_v come from the redshift-space data. Any degeneracies between cosmology and HOD parameters can be identified and marginalized over as well.

In §2 we outline the analytic model, presenting analytic expressions for $\xi(r_\sigma, r_\pi)$ by combining the HOD model for real-space clustering with the streaming model of equation (1). In §3 we detail the model for halo pairwise velocities, the key ingredient in the two-halo term, and calibrate it on the N-body simulations. §4 tests the model against the mock galaxy samples of Paper I, demonstrating that the model can recover the correct cosmological parameters from a wide va-

connecting the halo pair, *tangential* being in a direction orthogonal to the radial, and *line-of-sight* to be the direction from the observer. Velocities in these directions will be referred to as v_r , v_t , and v_z , respectively.

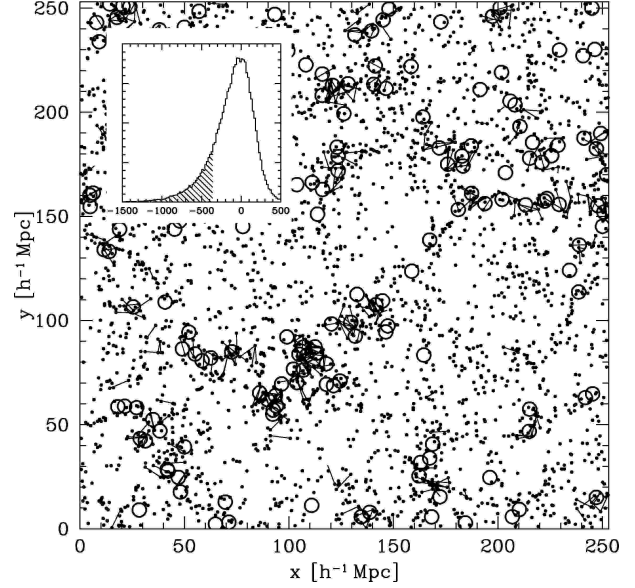


Figure 1. A slice through one simulation showing the locations of halos of different masses. Large open circles are halos of mass $M > 3 \times 10^{13}$. Small filled circles are halos of mass $\sim 2 \times 10^{12} h^{-1} \text{M}_\odot$. The inset box plots the probability distribution function (PDF) of radial velocities for the lower-mass halo pairs in the slice. The shaded regions of the histogram highlights the skewness toward high-velocity pairs. All halo pairs within the shaded region of the histogram are connected in the slice plot.

riety of cosmologies which produce significant degeneracies in redshift-space clustering. In §5 we summarize and discuss prospects for applying the model to current data sets.

2 MODELING THE CORRELATION FUNCTION IN REAL AND REDSHIFT SPACE

The real-space galaxy correlation function $\xi_R(r)$ can be calculated analytically with the HOD for a given galaxy sample and cosmology. In the HOD framework, galaxy clustering is separated into two distinct parts; pairs of galaxies within a single halo and those from two separate halos. The total correlation function is the sum of these two contributions (see, e.g., Berlind & Weinberg 2002; Cooray & Sheth 2002; Zheng 2004; and Tinker et al. 2005 for details on calculating the real-space correlation function).

The real-space one-halo term is written as

$$1 + \xi_{1h}(r) = \frac{1}{2\pi r^2 \bar{n}_g^2} \int_0^\infty dM \frac{dn}{dM} \frac{\langle N(N-1) \rangle_M}{2} \times \frac{1}{2R_{\text{vir}}(M)} F' \left(\frac{r}{2R_{\text{vir}}} \right), \quad (3)$$

where \bar{n}_g is the mean number density of galaxies, dn/dM is the halo mass function (here we use the formula presented in Jenkins et al. 2001), and $\langle N(N-1) \rangle_M$ is the average number of galaxy pairs in a halo of mass M . The function $F'(x)$ is the fraction of galaxy pairs at the scaled radius $x \equiv r/2R_{\text{vir}}$.

In practice, $F'(x)$ is different for galaxy pairs which involve the central galaxy and those between two satellite galaxies, and the calculation is separated into these two terms.

In real space, one-halo pairs dominate $\xi_R(r)$ at small scales. In redshift space, these pairs have large relative motions due to the virial dispersion of the halos they occupy, spreading these pairs out along the line of sight. We model the velocity distribution within each halo as an isotropic, isothermal Gaussian distribution, an approximation supported by numerical hydrodynamic simulations (Faltenbacher et al. 2004) and observational analysis of rich SDSS clusters (McKay et al., in preparation). The satellite galaxy velocity dispersion in a halo of mass M is proportional to the virial dispersion,

$$\sigma_{\text{sat}}^2 = \alpha_v^2 \sigma_{\text{vir}}^2 = \alpha_v^2 \frac{GM_h}{2R_{\text{vir}}}. \quad (4)$$

We define R_{vir} to be the radius at which the mean interior density of the halo is 200 times the background density, $R_{\text{vir}} = (4M_h/3\pi\bar{\rho}200)^{1/3}$. The constant of proportionality α_v is the galaxy velocity bias. For satellite pairs, the dispersion is $\sigma_{ss} = \sqrt{2}\sigma_{\text{sat}}$. For central galaxies, a natural assumption is that these galaxies are at rest with respect to the center of mass of the halo, or $\alpha_{vc} = 0$. In Paper I we tested this assumption, demonstrating that $\alpha_{vc} = 0.2$ has a negligible effect on redshift-space observables. We define $\sigma_{\text{cen}} = \alpha_{vc}\sigma_{\text{vir}}$, so the dispersion of central-satellite pairs is $\sigma_{cs} = (\alpha_v^2 + \alpha_{vc}^2)^{1/2}\sigma_{\text{vir}}$. Deviations from isotropy have little effect on $\xi(r_\sigma, r_\pi)$ for any physically reasonable value of the anisotropy, while non-isothermality resulting from spatial bias or unrelaxed systems can be modeled as an “effective” velocity bias parameter (Paper I).

In equation (3), the total number of one-halo pairs involves an integral over the halo mass function. At a given separation, the velocity PDF for one-halo pairs is a superposition of Gaussians weighted by the relative number of galaxy pairs from each halo of mass M . This superposition of Gaussians of varying dispersion makes the overall pairwise galaxy velocity dispersion approximately exponential (Sheth 1996), in accord with observational inferences (Davis & Peebles 1983; Hawkins et al. 2003).

The combination of equations (1) and (3) for central-satellite pairs is

$$\begin{aligned} \xi_{1h}^{(cs)}(r_\sigma, r_\pi) &= \frac{1}{2\pi\bar{n}_g^2} \int_0^\infty dM \frac{dn}{dM} \frac{\langle N_{\text{sat}} \rangle_M \langle N_{\text{cen}} \rangle_M}{2R_{\text{vir}}} \\ &\quad \int_{-\infty}^\infty F'_{cs} \left(\frac{\sqrt{r_\sigma^2 + z^2}}{2R_{\text{vir}}} \right) \frac{1}{\sqrt{2\pi}\sigma_{cs}} \\ &\quad \times \exp \left[\frac{-(r_\pi - z)^2}{2\sigma_{cs}^2} \right] \frac{dz}{(r_\sigma^2 + z^2)}, \end{aligned} \quad (5)$$

where $\langle N_{\text{cen}} \rangle_M$ and $\langle N_{\text{sat}} \rangle_M$ are the mean number of central and satellite galaxies for mass M , respectively. $F'_{cs}(x)$ is proportional to the halo density profile, which we assume to follow the form of Navarro et al. (1997, hereafter NFW). For satellite-satellite pairs, the one-halo term is

$$\begin{aligned} \xi_{1h}^{(ss)}(r_\sigma, r_\pi) &= \frac{1}{2\pi\bar{n}_g^2} \int_0^\infty dM \frac{dn}{dM} \frac{\langle N_{\text{sat}}(N_{\text{sat}} - 1) \rangle}{4R_{\text{vir}}} \\ &\quad \int_{-\infty}^\infty F'_{ss} \left(\frac{\sqrt{r_\sigma^2 + z^2}}{2R_{\text{vir}}} \right) \frac{1}{\sqrt{\pi}2\sigma_{\text{sat}}} \\ &\quad \times \exp \left[\frac{-(r_\pi - z)^2}{4\sigma_{\text{sat}}^2} \right] \frac{dz}{(r_\sigma^2 + z^2)}, \end{aligned} \quad (6)$$

where $\langle N_{\text{sat}}(N_{\text{sat}} - 1) \rangle$ is the second moment of the satellite occupation function, and $F'_{ss}(x)$ is the fraction of satellite-satellite pairs (see Sheth et al. 2001a for a derivation of $F_{cs}(x)$ and $F_{ss}(x)$ for the NFW profile). The full one-halo correlation function is $\xi_{1h}(r_\sigma, r_\pi) = \xi_{1h}^{(cs)} + \xi_{1h}^{(ss)}$.

The two halo term is most straightforward to calculate through a direct implementation of the equation (1),

$$1 + \xi_{2h}(r_\sigma, r_\pi) = \int_{-\infty}^\infty [1 + \xi_{2h}^R(r)] P_{2h}(v_z|r, \phi) dv_z. \quad (7)$$

where $\xi_{2h}^R(r)$ is the two-halo contribution to the real-space correlation function, $P_{2h}(v_z|r, \phi)$ is the line-of-sight velocity PDF of galaxy pairs from two distinct halos, and $\cos \phi = r_\sigma/r$. This PDF is a convolution of the line of sight PDF of halo pairwise velocities with the Gaussian distribution for galaxy velocities within each halo. $P_{2h}(v_z|r, \phi)$ is a pair-weighted average integrated over all possible combinations of halos;

$$\begin{aligned} P_{2h}(v_z|r, \phi) &= 2(\bar{n}_g')^{-2} \int_0^{M_{\text{lim},1}} dM_1 \frac{dn}{dM_1} \langle N \rangle_{M_1} \\ &\quad \int_0^{M_{\text{lim},2}} dM_2 \frac{dn}{dM_2} \langle N \rangle_{M_2} P_{g+h}(v_z|r, \phi, M_1, M_2), \end{aligned} \quad (8)$$

where P_{g+h} is the velocity PDF for galaxy pairs from halos of masses M_1 and M_2 . P_{g+h} includes both the internal motions of the galaxies within each halo and the relative motions of the halo centers of mass. The limits on each integral in equation (8) are determined by halo exclusion; halo pairs cannot be closer than the sum of their virial radii (i.e., $R_{\text{vir},1} + R_{\text{vir},2} \leq r$). At large separation, this effect is negligible because the largest collapsed objects have radii $\sim 2 h^{-1}\text{Mpc}$, and the limits of equation (8) approach infinity when r is large. At small scales, halo exclusion strongly influences the number of pairs. In equation (8), $M_{\text{lim},1}$ is the maximum halo mass such that $R_{\text{vir}}(M_{\text{lim},1}) = r - R_{\text{vir}}(M_{\text{min}})$ and $M_{\text{lim},2}$ is related to M_1 by $R_{\text{vir}}(M_{\text{lim},2}) = r - R_{\text{vir}}(M_1)$, where M_{min} is the minimum mass halo that can host a galaxy. The restricted number density, \bar{n}_g' , is the total number of two-halo galaxy pairs at separation r , also calculated using halo exclusion by

$$\bar{n}_g'^2 = \int_0^{M_{\text{lim},1}} dM_1 \frac{dn}{dM_1} \langle N \rangle_{M_1} \int_0^{M_{\text{lim},2}} dM_2 \frac{dn}{dM_2} \langle N \rangle_{M_2}. \quad (9)$$

We denote the velocity PDF of halo pairs as $P_h(v_z|r, \phi, M_1, M_2)$. This represents the center-of-mass motions only. Once the relative motions of the dark matter halos are determined, P_{g+h} is calculated by convolving P_h

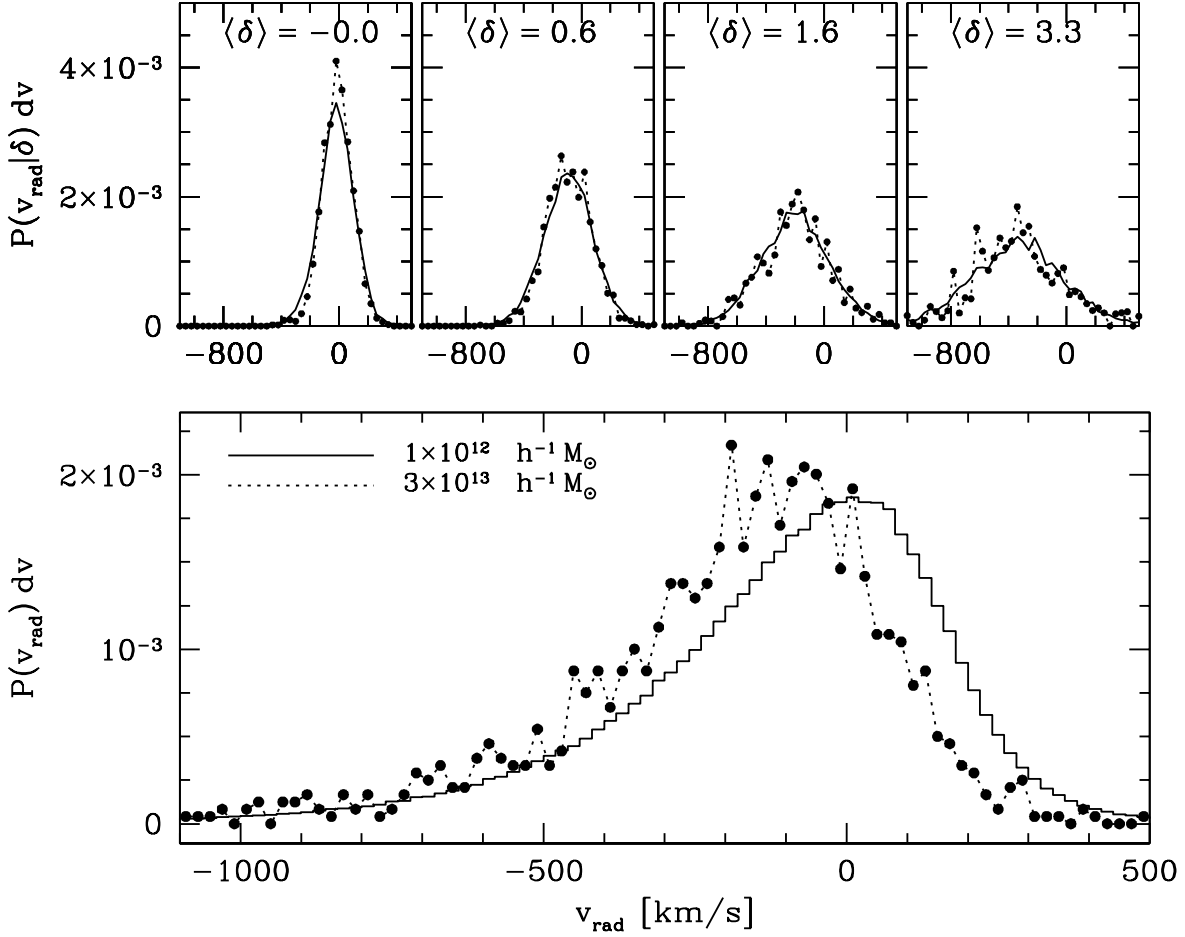


Figure 2. Velocity PDFs for halo pairs at different local densities. The top four panels plot PDFs as a function of local environment for low-mass halos (solid histograms) and high-mass halos (filled circles connected with dotted lines). The local density is calculated by a top-hat smoothing kernel centered on the midpoint between the halo pair, with radius equal to the halo separation. The bottom panel shows the unconditional velocity PDF for the same halos.

with the Gaussian describing the internal motions of the galaxies within the halos. The model for $P_h(v_z|r, \phi, M_1, M_2)$ is important both for capturing the behavior of the redshift-space correlation function in the transition region between the one- and two-halo terms and for correctly modeling distortions between quasi-linear to linear scales. We describe it in detail in the next section.

3 THE HALO VELOCITY MODEL

3.1 Conditional matter PDF

In §1 we listed the requirements an accurate model of $P_h(v)$ must satisfy. To meet these requirements, we use the N-body simulations from Paper I to explore halo velocity statistics. Our simulation set consists of five realizations of an inflationary Λ CDM cosmology with $\Omega_m = 0.1$ and

$\sigma_8 = 0.95$ at $z = 0$, using the public N-body code GADGET (Springel, Yoshida, & White 2001). We utilize outputs at higher redshifts to represent models at different values of σ_8 and Ω_m . Each simulation is 360^3 particles in a cubic volume $253 h^{-1}\text{Mpc}$ on a side, yielding a mass resolution of $9.64^{10} \times \Omega_m h^{-1}\text{M}_\odot$. The simulations have a power spectrum shape parameter $\Gamma = 0.2$ in the parameterization of Efstathiou et al. (1992), and a spectral index $n_s = 1$. See Paper I for further details regarding the simulations. Our fiducial cosmology is $\Omega_m = 0.3$, $\sigma_8 = 0.8$, corresponding to $z = 0.55$. Unless otherwise stated, N-body results will be using this output.

Figure 1 elucidates the complexity of $P_h(v|r, \phi, M_1, M_2)$. The inset box shows the PDF of radial velocities of halo pairs of mass $M_1 = M_2 \approx 2 \times 10^{12} h^{-1}\text{M}_\odot$ at a separation of $r \sim 10 h^{-1}\text{Mpc}$. Negative radial velocities are defined as the halos going toward one another. The PDF is not well described by either a Gaussian or an

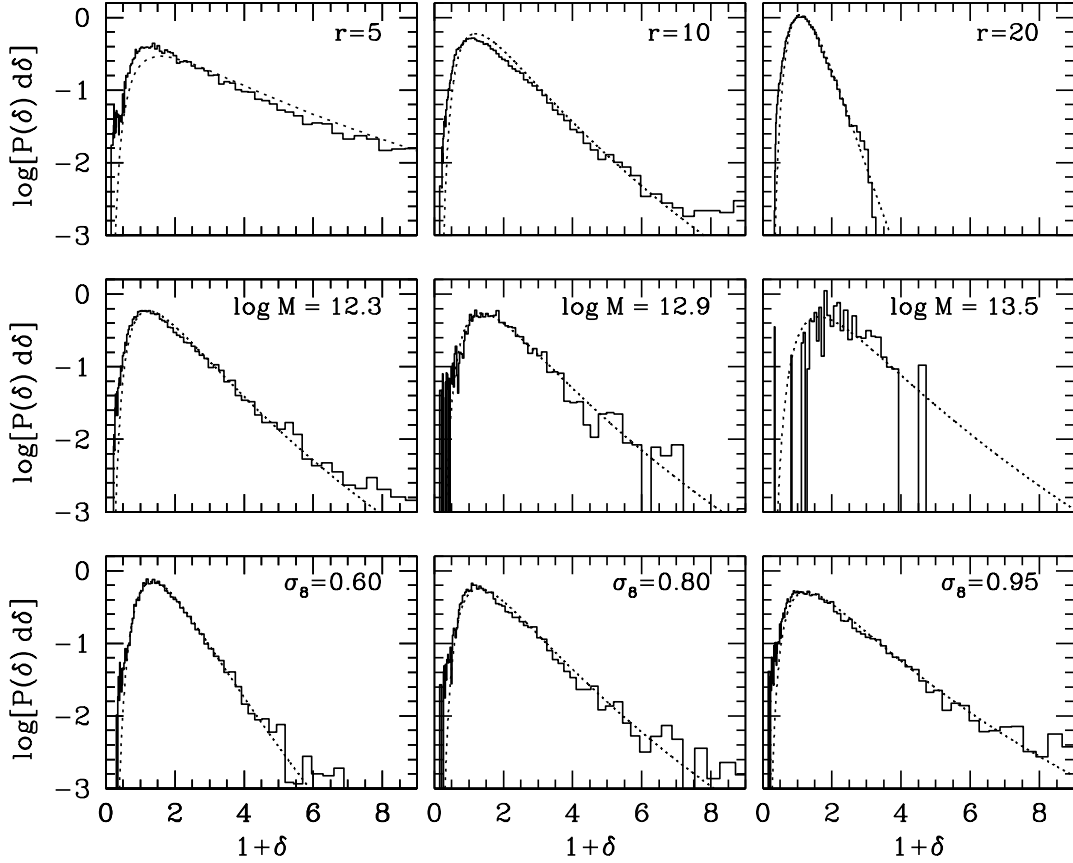


Figure 3. Comparison between the conditional matter PDFs measured from the simulations (*solid histograms*) and the model of Equation (11) (*dotted lines*). Top row: $P_m(\delta|r, M_1, M_2)$ for fixed mass ($10^{12} h^{-1} M_\odot$) and $\sigma_8 = 0.8$, but changing radius. Middle row: $P_m(\delta|r, M_1, M_2)$ for fixed radius ($10 h^{-1} \text{Mpc}$) and $\sigma_8 = 0.8$, but increasing halo mass. Bottom row: $P_m(\delta|r, M_1, M_2)$ for fixed mass ($10^{12.3} h^{-1} M_\odot$) and radius ($10 h^{-1} \text{Mpc}$), but changing σ_8 .

exponential. The shaded regions of the PDF highlights the skewed tail of halo pairs rapidly approaching each other. The outer panel plots the positions of these halos in a $40 h^{-1} \text{Mpc}$ slice through one realization. Small, filled circles indicate the $2 \times 10^{12} h^{-1} M_\odot$ halos of the inset histogram. The open circles in the plot represent high mass halos, $M > 3 \times 10^{13} h^{-1} M_\odot$. All pairs inside the shaded region of the histogram have been connected with a line. These high-velocity pairs are almost exclusively in regions that include a high mass halo. Because high mass halos preferentially occupy dense regions, we recover the well-known result that the non-linear halo velocity field is coupled to the non-linear density field. However, Figure 1 leads us to investigate the velocity PDF as a function of environment. In Figure 2, the lower panel plots the same PDF from Figure 1 for $10^{12} h^{-1} M_\odot$ halos at $r \sim 10 h^{-1} \text{Mpc}$. This panel also plots the PDF for $3 \times 10^{13} h^{-1} M_\odot$ at the same separation. The width of these mass bins is a factor of

two. The PDF for high-mass halos is noisier due to lower statistics, but it is apparent that the PDF for high-mass halos peaks at $v \sim -150 \text{ km s}^{-1}$, while the mode of the low-mass PDF is at zero. It is unlikely to find high-mass halos moving away from one another at this scale, while that probability is nearly 40% for low-mass halos.

The upper panels of Figure 2 show the PDFs for the same halos, now binned by local overdensity, $\delta \equiv \rho/\bar{\rho} - 1$. We calculate δ inside spheres of radius equal to the separation of the halo pairs, centered on the midpoint between the two halos. Setting the radius of the smoothing kernel equal to the halo separation allows for cleaner determination of the pair's environment. The four top panels span a range in mean local density of $\langle \delta \rangle \sim 0$ to 3. From these data the origin of the high-velocity tail is clear; the negative skewness arises from halo pairs which lie in dense environments. At $\delta = 0$, the velocity distribution is narrow and peaked at $v \approx 0 \text{ km s}^{-1}$. As δ increases, both the mean velocity and the dispersion

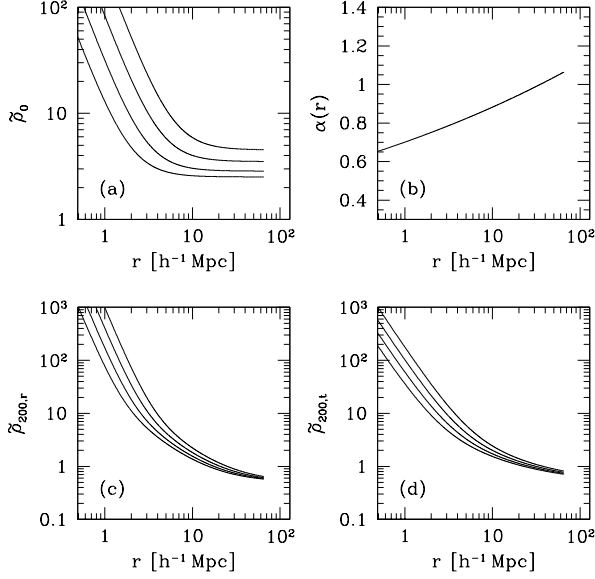


Figure 4. The scale and mass dependence of parameters of the two-halo velocity model. Each line represents of halo pair with mass ratio $M_2/M_1 = 4^i$, with $i = 0 - 3$ and $M_1 = 10^{12} h^{-1} M_\odot$. Panel (a): cutoff density scale for the 2-halo conditional matter PDF (Eq. [13]). Panel (b): Power-law index for the density-dependence of the pairwise velocity dispersion (Eq. [19]). There is only one line in this panel because there is no dependence on mass. Panel (c): Normalization of the density dependence of the pairwise radial velocity dispersion (Eq. [21]). Panel (d): Normalization of the density dependence of the pairwise tangential velocity dispersion (Eq. [22]).

increase as well. At fixed δ , the PDFs no longer show strong skewness or kurtosis; a Gaussian is a good approximation. Therefore the total distribution in the bottom panel can be modeled as a superposition of Gaussians weighted by the probability of finding a halo pair at a given δ .

At a given density, Figure 2 also demonstrates that the PDFs for high- and low-mass halos are very similar. It is the different distributions of local environments which leads to the differences in the total PDFs in the lower panel. We therefore propose the ansatz

$$P_h(v_{[r,t]}|r, M_1, M_2) = \int P_G(v_{[r,t]}|r, \delta, M_1, M_2) P_m(\delta|r, M_1, M_2) d\delta, \quad (10)$$

to model the radial and tangential pairwise motions of halos. In equation (10) P_G is a Gaussian, and $P_m(\delta|r, M_1, M_2)$ is the conditional matter density PDF in spheres of radius r centered on a halo pair of masses M_1 and M_2 . An ansatz of this type has been used to model one-point velocity statistics of halos and galaxies (Sheth & Diaferio 2001; Hamana et al. 2003). Although the PDFs in the upper panels of Figure 2 appear independent of halo mass, P_G varies moderately with mass at small scales because at small r the halos themselves contribute a large fraction of the total local mass. At scales

significantly larger than the halo radii, P_G becomes independent of mass.

The PDF for the unconditional matter distribution $P_m(\delta|r)$ is well fit by a lognormal distribution function with dispersion that varies with smoothing scale (e.g., Coles & Jones 1991; Kofman et al. 1994). The relationship between the halo mass function and the large-scale density field can also be quantified (e.g., Bond et al. 1991; Sheth & Tormen 2002; Pavlidou & Fields 2005). The conditional mass function can be roughly approximated as $n(M|\delta) \approx [1 + b(M)\delta] n(M)$ (Mo & White 1996), where $b(M)$ is the large-scale bias factor for halos of mass M (here we use the halo bias formula in Appendix A of Tinker et al. 2005). The distribution of densities at which a halo of a given mass can be found is roughly $P_m(\delta|r, M) \approx [1 + b(M)\delta] P_m(\delta|r)$ (Hamana et al. 2003). The term $[1 + b(M)\delta]$ effectively shifts the matter PDF to higher densities by an amount which depends on the bias of the halo.

The density distribution around pairs of halos, denoted as $P_m(\delta|r, M_1, M_2)$, is a murky theoretical problem with no obvious straightforward approach. To model $P_m(\delta|r, M_1, M_2)$ we truncate the unconditional matter distribution with an exponential cutoff at low densities, i.e.,

$$P_m(\delta|r, M_1, M_2) = A \exp \left[-\frac{\tilde{\rho}_0(r, M_1, M_2)}{\tilde{\rho}} \right] P_m(\delta|r), \quad (11)$$

where A is a normalization constant to make the total probability unity, $\tilde{\rho} \equiv 1 + \delta$, and $\tilde{\rho}_0$ is a density cutoff scale to be calibrated from the simulations. The one-point non-linear distribution function for the dark matter takes the form

$$P_m(\delta|r) = \frac{1}{2\pi\sigma_1^2} \exp \left[-\frac{[\ln(1 + \delta) + \sigma_1^2/2]^2}{2\sigma_1^2} \right] \frac{1}{1 + \delta}, \quad (12)$$

where $\sigma_1^2(r) = \ln[1 + \sigma_m^2(r)]$ and $\sigma_m(r)$ is the mass variance in top-hat spheres of radius r (e.g., Coles & Jones 1991; Kofman et al. 1994). To calculate $\sigma_m(r)$, we use the non-linear matter power spectrum of Smith et al. (2003). The cutoff density scale $\tilde{\rho}_0$ is

$$\tilde{\rho}_0 = \tilde{\rho}_1 [b(M_1) + b(M_2)] + \left(\frac{r}{r_0} \right)^{\alpha_0}. \quad (13)$$

At large scales, equation (13) is proportional to the sum of the halo bias factors. At small scales, where the masses of the halos themselves contribute significantly to local density, the mass contained within r cannot be below $M_1 + M_2$. Thus the cutoff density should scale roughly as $\tilde{\rho}_0 \propto (r/R_{\text{vir}})^{-3}$. From our N-body simulations, we find $\tilde{\rho}_1 = 1.41$, $\alpha_0 = -2.2$, and $r_0 = 9.4 R_{\text{vir},1}$, where $R_{\text{vir},1}$ is the virial radius of the larger halo of the halo pair, provide a good fit to the data. Figure 3 compares equation (11) to $P_m(\delta|r, M_1, M_2)$ measured from the N-body simulations. The top row of panels plots $\log[P(\delta)]$ measured in spheres centered on halo pairs of separations 5, 10, and 20 h^{-1} Mpc, for halos of mass $10^{12} h^{-1} M_\odot$. The N-body results, shown with the solid histograms, are lognormal in shape like the unconditional $P_m(\delta)$, with a dispersion that narrows as the smoothing scale increases. Dotted lines show equation (11), with $\tilde{\rho}_0$ calculated from equation (13) using the halo bias function

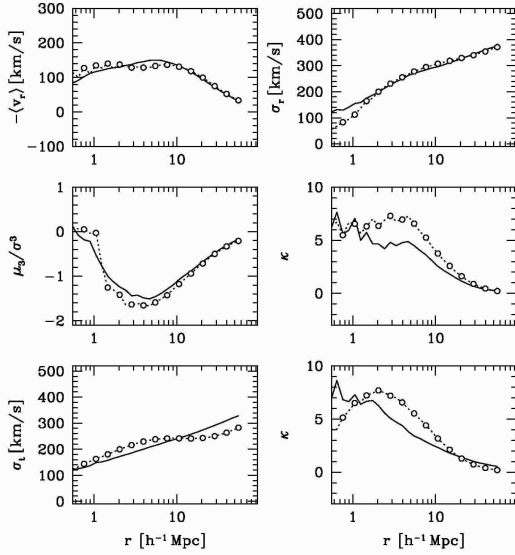


Figure 5. Comparison between the velocity statistics of N-body halos and the velocity model integrated over all halo masses. In all panels the solid line plots the N-body results and the open circles connected by dotted lines plots the model. The top four panels present the first four moments of the radial velocity PDFs as a function of scale: mean μ_r , dispersion σ_r , skewness μ_3/σ^3 , and kurtosis κ . The bottom two panels show the dispersion σ_t and kurtosis κ of the tangential PDFs. For proper comparison, the integrals over velocity for the moments are binned in the same manner as the N-body results and are truncated at the high and low velocities of the N-body statistics.

of Tinker et al. (2005). Equation (11) accurately tracks the change in $P_m(\delta|r, M_1, M_2)$ with smoothing scale.

The middle row of panels in Figure 3 compares the model to the N-body results for different halo masses at the same smoothing scale of $10 h^{-1}\text{Mpc}$. N-body halo pairs of mass $\sim 2 \times 10^{12} h^{-1}M_\odot$, which have large-scale bias of ~ 0.8 in our fiducial cosmology, reside on average in overdense regions, with $\langle\delta\rangle = 0.80$. As the mass increases by factors of 4 and 16 (with $b \sim 1.1$ and 1.5 , respectively), $\langle\delta\rangle$ increases to 1.00 and 1.36. The mean density calculated from equation (11) for each halo mass is 0.82, 1.02, and 1.32, in good agreement with the numerical results.

The bottom panel in Figure 3 isolates the effect of changing σ_8 on $P_m(\delta|r, M_1, M_2)$. The three panels present numerical results for $M \sim 5 \times 10^{12} h^{-1}M_\odot$ halos at $r \sim 10 h^{-1}\text{Mpc}$ for $\sigma_8 = 0.6, 0.8$, and 0.95 . In equation (12), the dependence of the matter distribution on the power spectrum is through the parameter $\sigma_m(r)$, which is proportional to σ_8 . As σ_8 increases, the dispersion in the unconditional $P_m(\delta|r)$ from equation (12) increases. The same is true for $P_m(\delta|r, M_1, M_2)$; the N-body results broaden substantially from $\sigma_8 = 0.6$ to 0.95 . The results from equation (11), plotted once again with the dotted lines, model the changes of $P_m(\delta|r, M_1, M_2)$ with σ_8 accurately. With three adjustable parameters, the quantities $\bar{\rho}_1$, α_0 and r_0 of equation (13), our model for the conditional matter PDF $P_m(\delta|r, M_1, M_2)$

reproduces the distinct effects of varying halo mass, smoothing scale, and power spectrum normalization.

3.2 Parameters of the Gaussian

For a halo pair at separation r and density δ , we approximate the radial velocity PDF as a distribution of the form

$$P(v_r|\delta, r, M_1, M_2) = \frac{1}{\sqrt{2\pi}\sigma_r} \exp\left[-\frac{(v - \mu_r)^2}{2\sigma_r^2}\right]. \quad (14)$$

Both the mean μ_r and the dispersion σ_r of the radial velocity PDF depend on δ . The PDF for tangential velocities is also a Gaussian, but with dispersion σ_t and zero mean. At large scales, or at negative density contrast, μ_r is well described by linear theory,

$$\mu_{\text{lin}}(\delta, r) = -H r \Omega_m^{0.6} \frac{\delta}{3}. \quad (15)$$

At small scales, μ_r is approximated by the non-linear spherical collapse model (see, e.g., Peacock 1999). In this model, the dependence of the velocity perturbation on density is expressed parametrically as

$$\delta = \frac{9(\gamma - \sin \gamma)^2}{2(1 - \cos \gamma)^3} - 1 \quad (16)$$

$$u = \frac{3 \sin \gamma (\gamma - \sin \gamma)}{(1 - \cos \gamma)^2} - 1. \quad (17)$$

The mean radial velocity is

$$\mu_{\text{sc}}(\delta, r) = H r \Omega_m^{0.6} u(\delta) \exp[-(4.5/r\tilde{\rho})^2], \quad (18)$$

where the exponential term is added to better match the N-body results at the smallest scales but has little influence on the overall behavior of μ_{sc} . Investigation of our N-body results shows that the spherical collapse model best describes the N-body simulations at $r \lesssim 4 h^{-1}\text{Mpc}$, while linear theory is an excellent description of the results for $r \gtrsim 20 h^{-1}\text{Mpc}$. In the transition region, we express μ_r as a weighted mean of equations (15) and (18), which smoothly transitions between the two regimes. The weighting factor, w_μ increases linearly from 0 to 1 in $\ln(r)$ in the range $4 \leq r \leq 20 h^{-1}\text{Mpc}$, with $\mu_r = w_\mu \mu_{\text{sc}} + (1 - w_\mu) \mu_{\text{lin}}$.

Recalling Figure 2, the skewness of the radial velocity PDF arises from the combination of halo pairs in high-density regions, which have a large streaming velocity and high dispersion, with halo pairs in mean- to low-density regions, which have low mean streaming velocity (relative to Hubble flow) and small dispersion. In our N-body simulations, the skewness of the radial velocity distribution does not monotonically increase as halo separation decreases. As halo pairs become close, of order twice the sum of their virial radii, the skewness decreases and the PDF becomes more symmetric. Because μ_{sc} diverges rapidly as δ becomes large, the skewness of the model will always increase with decreasing r . To compensate for this effect, we enforce the condition that at $r = 4R_{\text{vir},1}$, μ_r is held constant for all δ at the value of the most probable δ for that separation, removing the skewness entirely. In the full halo+galaxy PDF, this change from skewed to symmetric distribution functions is

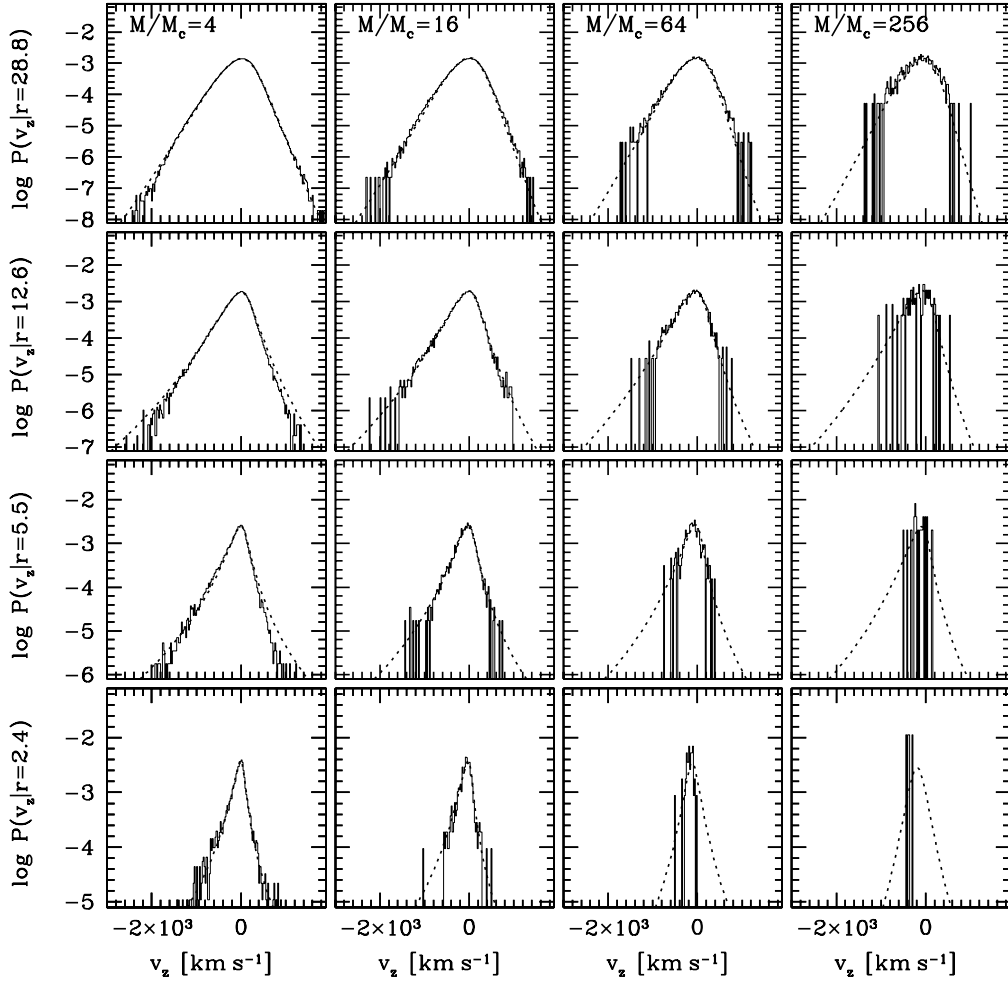


Figure 6. Comparison between line-of-sight velocity PDFs measured from the simulations and from the analytic model. Solid histograms show the N-body results and dotted lines plot the model calculations. The sixteen panels create a grid in which halo mass increases from left to right and separation increases from bottom to top. Halo pairs are all of equal masses and at an angle of 45° with respect to the line of sight.

smoothed out in scale through the change in $R_{\text{vir},1}$ with halo mass.

It is clear from Figure 2 that the velocity dispersion also depends on the local density. Hamana et al. (2003) show that the one-point velocity dispersion of halos is described by a power law, i.e. $\sigma_v \propto (1 + \delta)^\alpha$. We find that this is also true of the pairwise velocities but, that both the normalization and index of the power law are functions of scale. The power-law index varies weakly with radius, and is modeled by

$$\alpha(r) = \left(\frac{r}{35 h^{-1} \text{Mpc}} \right)^{0.1}. \quad (19)$$

In linear theory the dispersion of halo space velocities scales with cosmology as $\Omega_m^{0.6} \sigma_8$. We parameterize the halo

velocity dispersions in terms of the overdensity $\tilde{\rho}_{200}$ at which the dispersion is 200 km s^{-1} in our fiducial cosmology:

$$\sigma_{(r,t)} = 200 \left(\frac{\Omega_m}{0.3} \right)^{0.6} \left(\frac{\sigma_8}{0.8} \right) \left(\frac{\tilde{\rho}}{\tilde{\rho}_{200}(r,t)} \right)^\alpha \text{ km s}^{-1}, \quad (20)$$

where $\tilde{\rho}_{200}(r,t)$ is a function of M_1 , M_2 , and r . We find that the following formulas provide a reasonable description of the radial and tangential velocity dispersions in the simulations:

$$\tilde{\rho}_{200,r}(M_1, M_2, r) =$$

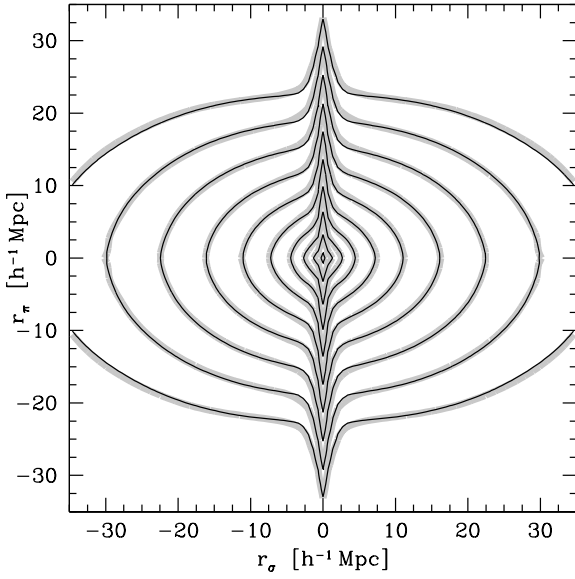


Figure 7. $\xi(r_\sigma, r_\pi)$ for HOD3 in Table 1. The contours plot constant amplitude of $\xi(r_\sigma, r_\pi)$, separated by powers of 1.7. The outermost contour is $1.7^{-5} = 0.07$. Thick gray lines show the N-body results and thin black lines are the model calculation.

$$\left(\frac{r}{5.0R_{\text{vir},1}^{1/2}}\right)^{-4.0} + \left(\frac{r}{11.5R_{\text{vir},0}^{1/2}}\right)^{-1.3} + 0.50, \quad (21)$$

$$\tilde{\rho}_{200,t}(M_1, M_2, r) = \left(\frac{r}{7.2R_{\text{vir},1}^{1/2}}\right)^{-2.5} + \left(\frac{r}{12.6R_{\text{vir},0}^{1/2}}\right)^{-0.8} + 0.48, \quad (22)$$

where $R_{\text{vir},0} = R_{\text{vir},1} + R_{\text{vir},2}$. The units of r and R_{vir} in equations (21) and (22) are $h^{-1}\text{Mpc}$. The mass dependence again enters with the virial radii of the halos, but the dependence on halo mass is weaker than for the density distribution in equation (13). Figure 4 shows the radial dependence of the four model parameters which must be calibrated to the simulations, $\tilde{\rho}_0$, α , $\tilde{\rho}_{200,r}$, and $\tilde{\rho}_{200,t}$, from equations (13), (19), (21), and (22), respectively. The different lines in each panel are for halo pairs M_1 and M_2 , where $M_1 = 10^{12} h^{-1} M_\odot$, and $M_2/M_1 = 4^i$, and $i = 0 - 3$. At large scales, the dependence on halo mass becomes negligible except when it enters in the bias factor used in the cutoff of the density PDF. At these scales, the value of $\tilde{\rho}_{200}$ approaches a constant for both tangential and radial velocities indicating that the velocity dispersion becomes independent of scale and mass.

Using this model, we integrate over all halo pairs and calculate equation (8) for halos alone, without any contribution from galaxies (i.e. $\langle N \rangle_M = 1$). For this special case, equation (8) becomes

$$P_h(v|r) = 2(\bar{n}'_h)^{-2} \int_0^{M_{\text{lim},1}} dM_1 \frac{dn}{dM_1}$$

$$\int_0^{M_{\text{lim},2}} dM_2 \frac{dn}{dM_2} P_h(v|r, M_1, M_2) \quad (23)$$

where v can refer to either v_r or v_t , and \bar{n}'_h is the number density of halos allowed by halo exclusion, in analogy to equation (9). Equation (23) allows a direct comparison to our N-body simulations. Figure 5 shows the first four moments of the halo velocity PDF as a function of scale for the radial velocities, and the first two even moments for the tangential velocities, for our fiducial cosmology. The N-body results are shown with the solid line and the model is the open circles connected by the dotted line. For calculating the velocity moments with the model, we use the model value at the center of each bin that has a non-zero probability in the N-body distribution and set the more extended wings of $P(v)$ to zero. The contribution from the high- v wings makes little difference for the comparison of the first two moments, but it noticeably affects the comparison of the skewness and kurtosis to the N-body results.

The mean and dispersion of the radial velocities are accurately described by the model. For the skewness, denoted as μ_3/σ^3 with $\mu_3 = \sum (v_i - \mu)^3/N$, the N-body results demonstrate the previous statement that the asymmetry is minimal at large separation, reaches a peak at intermediate scales near $4 h^{-1}\text{Mpc}$, and turns over to become nearly zero at $r \lesssim 1 h^{-1}\text{Mpc}$. The model describes this behavior well, reaching a peak at the same location and reducing to zero at $r = 1 h^{-1}\text{Mpc}$. The kurtosis, defined as $\kappa = \mu_4/\sigma^4 - 3$ with $\mu_4 = \sum (v_i - \mu)^4/N$, approaches zero at large scales for both the tangential and radial velocities, and monotonically increases with decreasing r to a value of $\kappa \approx 7$ at $r \approx 1 h^{-1}\text{Mpc}$ (for reference, $\kappa = 2$ for an exponential distribution). The kurtosis is moderately over-predicted at intermediate scales in the model, but both the sign and slope of the trend with radius are correct. As we will show later in §5, this small discrepancy with the fourth moment does not adversely affect the accuracy of the $\xi(r_\sigma, r_\pi)$ model.

3.3 $P_h(v_z)$ as a function of angle

For a halo pair at angle ϕ , the line of sight relative velocity is $v_z = v_r \sin \phi + v_t \cos \phi$, where $\cos \phi = r_\sigma/r$. Unfortunately, knowing the radial and tangential velocity PDFs independently does not allow one to compute $P(v_z)$ because the radial and tangential velocities are correlated; if the radial infall velocity is high, the tangential velocity is also likely to be high. However, this correlation is accounted for by the density dependence of the PDFs in our model, and at fixed δ the distributions $P(v_r)$ and $P(v_t)$ are independent. The line-of-sight distributions can then be computed from the appropriate convolution,

$$P_h(v_z|\phi, \delta, M_1, M_2, r) = \int_{-\infty}^{\infty} P_h(v_t|\phi, \delta, M_1, M_2, r) P_h(v_r|\phi, \delta, M_1, M_2, r) dv_t, \quad (24)$$

where $v_r = (v_z - v_t \cos \phi)/\sin \phi$, to obtain

$$P_h(v_z|\phi, \delta, M_1, M_2, r) = \frac{1}{\sqrt{2\pi}} (\sigma_t^2 \cos^2 \phi + \sigma_r^2 \sin^2 \phi)^{-1/2} \times \exp \left[\frac{-(v_z - \sin \phi \mu_r)^2}{2(\sigma_t^2 \cos^2 \phi + \sigma_r^2 \sin^2 \phi)} \right]. \quad (25)$$

Inspection of equation (25) produces the expected result that at $\phi = \tan \phi = \sin \phi = 0$, the expression reduces to a zero-mean Gaussian with dispersion σ_t . For $\phi = \pi/2$, it reduces to equation (14).

Rather than compare the moments of $P_h(v_z)$ from the model to the N-body simulations at a given ϕ , since they appear much as they do in Figure 5, instead we compare the PDFs themselves for several masses and separations at an angle of 45° . The sixteen panels of Figure 6 represent a grid of models where each row is a different separation and each column is a different mass. In each column, the halo pairs are $M_1 = M_2 = 4^i M_c$, with $i = 1 - 4$, and $M_c = 10^{12} h^{-1} M_\odot$. In each panel the solid histogram represents the N-body results and the dotted line plots the model calculation. The agreement between the model and the N-body results is excellent wherever the N-body statistics are good. The model reproduces the numerical results over an order of magnitude variation in radius and almost two decades in halo mass.

3.4 Combining halos and galaxies

Because the halo PDF at fixed δ , r , and halo masses is a Gaussian, internal motions of the galaxies can be included by adding the galaxy dispersion to the halo velocity dispersion in quadrature. As in the one-halo term, pairs involving central and satellite galaxies must be treated separately once again. In the two-halo term, there are four distinct types of pairs with four velocity dispersions: central-central pairs, satellite-satellite pairs, and satellite galaxies from M_1 paired with the central galaxy of M_2 and vice versa. The four velocity dispersions are

$$\begin{aligned} \sigma_1^2 &= \sigma_h^2 + [\sigma_{\text{vir}}^2(M_1) + \sigma_{\text{vir}}^2(M_2)] \alpha_{vc}^2 \\ \sigma_2^2 &= \sigma_h^2 + [\sigma_{\text{vir}}^2(M_1) + \sigma_{\text{vir}}^2(M_2)] \alpha_v^2 \\ \sigma_3^2 &= \sigma_h^2 + [\alpha_{vc}^2 \sigma_{\text{vir}}^2(M_1) + \alpha_v^2 \sigma_{\text{vir}}^2(M_2)] \\ \sigma_4^2 &= \sigma_h^2 + [\alpha_{vc}^2 \sigma_{\text{vir}}^2(M_2) + \alpha_v^2 \sigma_{\text{vir}}^2(M_1)], \end{aligned} \quad (26)$$

where $\sigma_h^2 = \sigma_t^2 \cos^2 \phi + \sigma_r^2 \sin^2 \phi$. The complete PDF is a linear combination of these four Gaussian functions,

$$P_{g+h}(v_z|\phi, r, M_1, M_2, \delta) = \sum_{i=1}^4 \frac{w_i}{\sqrt{2\pi}\sigma_i} \exp \left[\frac{-(v_z - \mu_r \sin \phi)^2}{2\sigma_i^2} \right], \quad (27)$$

where each term is weighted by the relative number of pairs of each type, i.e.,

$$\begin{aligned} w_1 &= \langle N_{\text{cen}} \rangle_{M_1} \langle N_{\text{cen}} \rangle_{M_2} / \langle N \rangle_{M_1} \langle N \rangle_{M_2} \\ w_2 &= \langle N_{\text{sat}} \rangle_{M_1} \langle N_{\text{sat}} \rangle_{M_2} / \langle N \rangle_{M_1} \langle N \rangle_{M_2} \\ w_3 &= \langle N_{\text{cen}} \rangle_{M_1} \langle N_{\text{sat}} \rangle_{M_2} / \langle N \rangle_{M_1} \langle N \rangle_{M_2} \\ w_4 &= \langle N_{\text{sat}} \rangle_{M_1} \langle N_{\text{cen}} \rangle_{M_2} / \langle N \rangle_{M_1} \langle N \rangle_{M_2}. \end{aligned} \quad (28)$$

To obtain the full galaxy+halo PDF for a pair of halos M_1 and M_2 , equation (27) is weighted by $P_m(\delta|r, M_1, M_2)$ and integrated over all densities, i.e.,

$$P_{g+h}(v_z|\phi, r, M_1, M_2) = \int_{-1}^{\infty} P_{g+h}(v_z|\phi, r, M_1, M_2, \delta) P_m(\delta|r, M_1, M_2) d\delta. \quad (29)$$

To complete the calculation of the two-halo velocity PDF, equation (29) is integrated over all combinations of halo masses as in equation (8), which gives $P_{2h}(v_z|\phi, r)$ (note that the subscript $2h$ refers to two-halo galaxy pairs, as in §2). This PDF is used in the two-halo streaming model, equation (7). Once the total velocity PDF has been calculated and tabulated as a function of separation and angle, $\xi_{1h}(r_\sigma, r_\pi)$ is calculated from equations (5) and (6) and $\xi_{2h}(r_\sigma, r_\pi)$ from equation (7).

4 RESULTS

Although one-dimensional diagnostics are preferable when analyzing observational measurements of redshift-space distortions, it is worthwhile to demonstrate the ability of the model to reproduce the overall features of the two-dimensional $\xi(r_\sigma, r_\pi)$. Figure 7 plots $\xi(r_\sigma, r_\pi)$ for both the N-body results and model for our central model, HOD3 in Table 1, plotted as contours of constant correlation in the $r_\sigma - r_\pi$ plane. The thick gray contours represent the N-body data, averaged over the fifteen orthogonal projections of the five realizations, and the thin black lines plot the model results. The contours are separated by powers of 1.7, with the outermost contour representing $1.7^{-5} = 0.07$. The coherent infall of matter into overdense regions is present in the flattening of the contours on large scales. In the absence of this infall, the contours would be concentric circles at these scales. At small scales the FOG effect is shown by the sharp elongation of contours at $r_\sigma \lesssim 2 h^{-1} \text{Mpc}$. The model accurately reproduces both the large- and small-scale effects seen in the N-body results.

Although it is possible to compare model predictions directly to the observed two-dimensional correlation function $\xi(r_\sigma, r_\pi)$, this is not preferred due to the complexity of the error analysis. There is a strong covariance between data points, making it difficult to accurately estimate the covariance matrix of the measurements due to the large number of data points. Using the two-dimensional data set also makes it difficult to isolate constraints on the cosmological parameters from constraints on the HOD parameters. We proceed instead by extracting one-dimensional observables from the two-dimensional data, observables that are more easily interpreted in terms of the parameters Ω_m , σ_8 , and α_v .

4.1 Redshift-space observables

In Paper I we described three observables for the correlation function. The first two, based on multipoles of $\xi(r_\sigma, r_\pi)$,

Table 1. Properties of the Simulations and HOD Parameters

| Model | σ_8 | $M_{\min} [h^{-1}M_{\odot}]$ | $M_1 [h^{-1}M_{\odot}]$ | α_{sat} | $\Omega_m(\beta = 0.46)$ | α_v |
|-------|------------|------------------------------|-------------------------|-----------------------|--------------------------|------------|
| HOD1 | 0.95 | 1.12×10^{12} | 2.81×10^{13} | 0.934 | 0.24 | 1.109 |
| HOD2 | 0.90 | 1.12×10^{11} | 2.75×10^{13} | 0.959 | 0.26 | 1.076 |
| HOD3 | 0.80 | 1.09×10^{12} | 2.51×10^{13} | 1.005 | 0.30 | 1.000 |
| HOD4 | 0.70 | 1.08×10^{12} | 2.24×10^{13} | 1.109 | 0.36 | 0.906 |
| HOD5 | 0.60 | 1.06×10^{12} | 1.93×10^{13} | 1.199 | 0.47 | 0.797 |

Note— All masses have been scaled to $\Omega_m = 0.3$. When we scale an HOD to a different value of Ω_m , the values of M_{\min} and M_1 scale in proportion to Ω_m . Values in the sixth and seventh columns are the parameters of the HOD models used in §4.3, which have $\beta = 0.46$ and the same finger-of-god strength for all five models.

emphasized large-scale distortions because they have predictions in linear theory. The multipoles of the correlation function are expressed as

$$\xi_l(r) = \frac{2l+1}{2} \int_{-1}^{+1} \xi(r_\sigma, r_\pi) P_l(\mu) d\mu, \quad (30)$$

where $r^2 = r_\sigma^2 + r_\pi^2$, $\mu = r_\pi/r$, and $P_l(\mu)$ is the Legendre polynomial of order l . The ratio of the monopole to the real-space correlation function,

$$\xi_{0/R}(r) = \frac{\xi_0(r)}{\xi_R(r)}, \quad (31)$$

is predicted in linear theory to be a constant value larger than one, but non-linearities in the velocity field suppress small-scale redshift-space clustering, driving this ratio to zero as r becomes small. In Paper I, we restricted our use of this diagnostic to the asymptotic value at $r \geq 10 h^{-1}\text{Mpc}$, but small scales contain additional information, and in this analysis we will make use of the full range of r .

The quadrupole moment of the correlation function is defined as

$$Q_\xi(r) = \frac{\xi_2(r)}{\xi_0(r) - \xi_0(r)} \quad (32)$$

where $\bar{\xi}_0(r)$ is the volume averaged monopole,

$$\bar{\xi}_0(r) = \frac{3}{r^3} \int_0^r \xi_0(s) s^2 ds. \quad (33)$$

In the numerical results of Paper I, this diagnostic also has an asymptotic value at large scales that is roughly consistent with its linear theory prediction, but due to the higher-order multipole, equation (32) is more sensitive to the galaxy velocity dispersion, and non-linearities affect this diagnostic at larger r than $\xi_{0/R}$. For cosmologies that produce strong redshift distortions, e.g. $\beta \gtrsim 0.6$, Q_ξ does not reach a flat plateau even at $40 h^{-1}\text{Mpc}$, putting the linear theory regime outside the range of high precision measurements.

To quantify small-scale distortions, Paper I focused on the behavior of $\xi(r_\pi)$ at fixed, small r_σ . We define the quantity $r_{\xi/2}$ as the value of r_π at which the correlation function falls by a factor of two from its value at $r_\pi = 0$, or

$$\frac{\xi(r_{\xi/2})}{\xi(0)} = \frac{1}{2}. \quad (34)$$

The quantity $r_{\xi/2}$ can be thought of as a characteristic length scale for FOGs. At $r \sim 0.1 h^{-1}\text{Mpc}$, $r_{\xi/2}$ depends

on the parameter combination $\Omega_m \alpha_v^2$ and is nearly independent of σ_8 . At intermediate scales, $r \sim 1 h^{-1}\text{Mpc}$, $r_{\xi/2}$ is highly sensitive to σ_8 because the number of one-halo pairs at this scale depends on the shape of the halo mass function at large masses. For the approach of Paper I, measuring $r_{\xi/2}$ at $r_\sigma = 0.1 h^{-1}\text{Mpc}$ is beneficial because it provides a simple relation to constrain $\Omega_m \alpha_v^2$.

The form of the HOD used in Paper I is simple in its parameterization; halos above a minimum mass M_{\min} have a central galaxy located at the center of mass of the host halo, while satellite galaxies have a mean occupation number that scales as a power law with the host halo mass, i.e. $\langle N_{\text{sat}} \rangle_M = (M/M_1)^{\alpha_{\text{sat}}}$. Therefore the mean occupation function is

$$\langle N \rangle_M \equiv \langle N_{\text{cen}} \rangle_M + \langle N_{\text{sat}} \rangle_M = 1 + \left(\frac{M}{M_1} \right)^{\alpha_{\text{sat}}} \quad (35)$$

for $M \geq M_{\min}$, and $\langle N \rangle_M = 0$ below M_{\min} . The dispersion of satellite galaxies about $\langle N_{\text{sat}} \rangle_M$ is assumed to be Poisson, motivated by both numerical results (Kravtsov et al. 2004; Zheng et al. 2005) and observational studies (Lin et al. 2004). The mean occupation of central galaxies is a step function with no scatter. This parameterization has only two free parameters² but still has enough freedom to model the observed $w_p(r_p)$ of SDSS galaxies (Zehavi et al. 2005). Table 1 lists the HOD parameters for the five values of σ_8 considered in Paper I, with all masses scaled to $\Omega_m = 0.3$. These parameters were chosen such that $\xi_R(r)$ was nearly identical for all values of σ_8 . We make mock galaxy distributions by populating the N-body halos with galaxies according to equation (35). Satellite galaxies are placed randomly throughout the halo following the appropriate NFW profile for each mass and cosmology, calculated with the model of Bullock et al. (2001). Velocities are selected randomly from a Gaussian distribution with dispersion given by equation (4). See Paper I for further details.

Figure 8 plots the three redshift-space diagnostics for the central model. In all panels, the filled circles represent the N-body data, the solid line plots the model calculation, and the dotted line represents the dispersion model (eq. [2])³ for $\beta = 0.46$ and the best-fit value of σ_v of 418 km s^{-1} . Note

² M_{\min} is set by the space density of galaxies once M_1 and α_{sat} are chosen.

³ We use the implementation of the dispersion model in configuration space as shown in Hawkins et al. (2003).

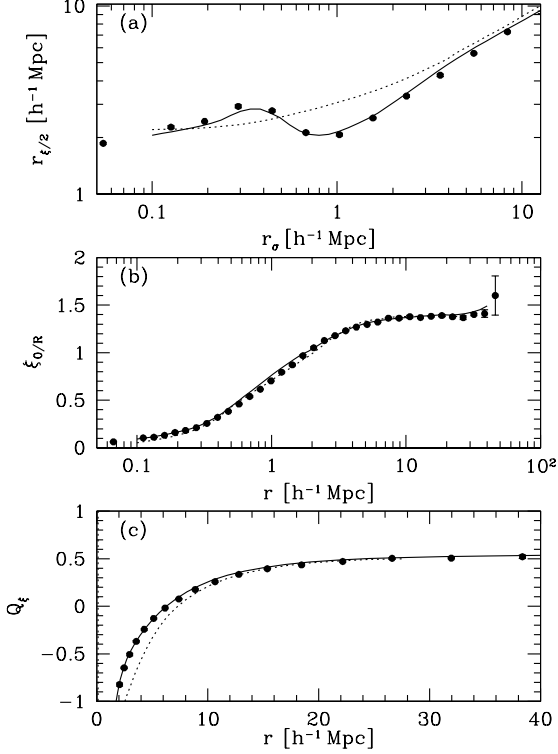


Figure 8. One-dimensional measures of redshift-space clustering. In each panel, the filled circles show the results of HOD3 from the N-body simulations (see Table 1). Error bars are shown, but at most r are smaller than the point size. Solid lines show the model calculations, and dotted lines show the best-fit dispersion model with $\sigma_v = 418 \text{ km s}^{-1}$. Panel (a) plots $r_{\xi/2}$ against r_{σ} . Panel (b) plots $\xi_{0/R}$ against r . Panel (c) plots Q_{ξ} against r .

that our model does *not* have a parameter (like σ_k) adjusted to match the redshift-space distortions, and in that sense has less freedom to reproduce the data, though the formulas describing the halo pairwise velocities were calibrated on the simulations. Error bars on the N-body results are calculated from the dispersion of the five simulations divided by $\sqrt{4}$ to yield the error in the mean, but they are generally too small to be seen outside the plot symbols.

Figure 8a plots the results for $r_{\xi/2}$ as a function of transverse separation. Both the N-body results and the model show a wave pattern that results from the transition in $\xi_R(r)$ from the one-halo to two-halo term (see §5 in Paper I). As the dominant source of pairs shifts from one-halo pairs in high-mass systems to two-halo pairs in low-mass halos, the galaxy velocity dispersion decreases sharply (Slosar et al. 2006; Tinker et al. 2006b). The dispersion model shows no such wave pattern and is a poor fit to the N-body data, demonstrating the inability of a simple, scale-independent velocity parameter to describe small-scale galaxy motions.

Figure 8b plots $\xi_{0/R}$ as a function of $\log(r)$. The large-scale infall amplifies the clustering, making $\xi_{0/R} > 1$ at $r \gtrsim 4 h^{-1} \text{ Mpc}$, while non-linearities suppress clustering, driving ξ_0/ξ_R to zero at small separation. Because $\xi_0(r)$ is the lowest order multipole, it is least sensitive to the higher order

moments of the velocity field. Thus, both the HOD model and the dispersion model provide good fits to the N-body results.

Figure 8c plots Q_{ξ} as a function of r . Non-linearities become apparent in the quadrupole at a larger scale than in the monopole; although Q_{ξ} flattens to a horizontal asymptote at large scales, the data deviate significantly from this asymptote at $r \lesssim 20 h^{-1} \text{ Mpc}$, and Q_{ξ} becomes negative at $r \sim 6 h^{-1} \text{ Mpc}$. Both the HOD model and the dispersion model reproduce the large-scale behavior, but the dispersion solution is a poor fit at $r \lesssim 10 h^{-1} \text{ Mpc}$. The HOD model is accurate at all scales.

Figure 9 plots the results of the N-body simulations for these same diagnostics but with variations in the $(\Omega_m, \sigma_8, \alpha_v)$ parameter space. In each panel, the circles plot the N-body data, with filled and open circles representing the high and low values of the isolated parameter, respectively. The solid and dotted lines are the model results for the high and low parameter values, respectively. The bottom row shows the results for the highest and lowest values of σ_8 considered in Paper I (0.6 and 0.95), with $\Omega_m = 0.3$ and $\alpha_v = 1.0$. The middle row presents the extreme values of Ω_m (0.1 and 0.5), with $\sigma_8 = 0.8$ and $\alpha_v = 1$. The top row presents results for setting α_v to 0.8 and 1.2 while keeping Ω_m and σ_8 fixed at their central values. In all cases, the HOD model accurately tracks the changes in the redshift-space diagnostic with changes in cosmological parameters, despite having no adjustable parameters of its own.

4.2 Parameter Recovery

In Paper I we concluded that combining redshift-space information from multiple scales can break degeneracies and allow determination of Ω_m , σ_8 , and α_v . Models along the linear theory degeneracy axis, $\Omega_m^{0.6} \sigma_8 = \text{const.}$, have nearly identical large-scale redshift distortions that can mask significant changes in cosmology. Models along the degeneracy axis controlling satellite galaxy velocities, $\Omega_m \alpha_v^2 = \text{const.}$, have the same value of $r_{\xi/2}$ when measured at $r_{\sigma} \lesssim 0.2 h^{-1} \text{ Mpc}$. Thus it is possible for widely varying cosmologies to produce the same large-scale anisotropies and the same small-scale FOGs. Despite these degeneracies, information from intermediate scales, where the one-halo to two-halo transition occurs, is able to break these degeneracies.

To test the ability of the model to recover the correct cosmological parameters, we use this set of large scale/small scale degenerate models as the input data. The values of Ω_m and α_v for each model are listed in columns 6 and 7 of Table 1. The models are scaled to values of Ω_m such that $\beta = 0.46$ for all five HODs, and values of α_v are chosen such that $r_{\xi/2} \approx 2.1 h^{-1} \text{ Mpc}$ at $r_{\sigma} = 0.1 h^{-1} \text{ Mpc}$. All models have approximately the same real-space correlation function (see Figure 2 in Paper I). We use four observables; $\xi_R(r)$, $\xi_{0/R}$, Q_{ξ} , and $r_{\xi/2}$, with diagonal error bars calculated from the standard deviation of the mean of the five simulations. We also add a systematic error to the model of 3% in each quantity to prevent data points with small errors from dominating the χ^2 minimization. With this systematic error, the

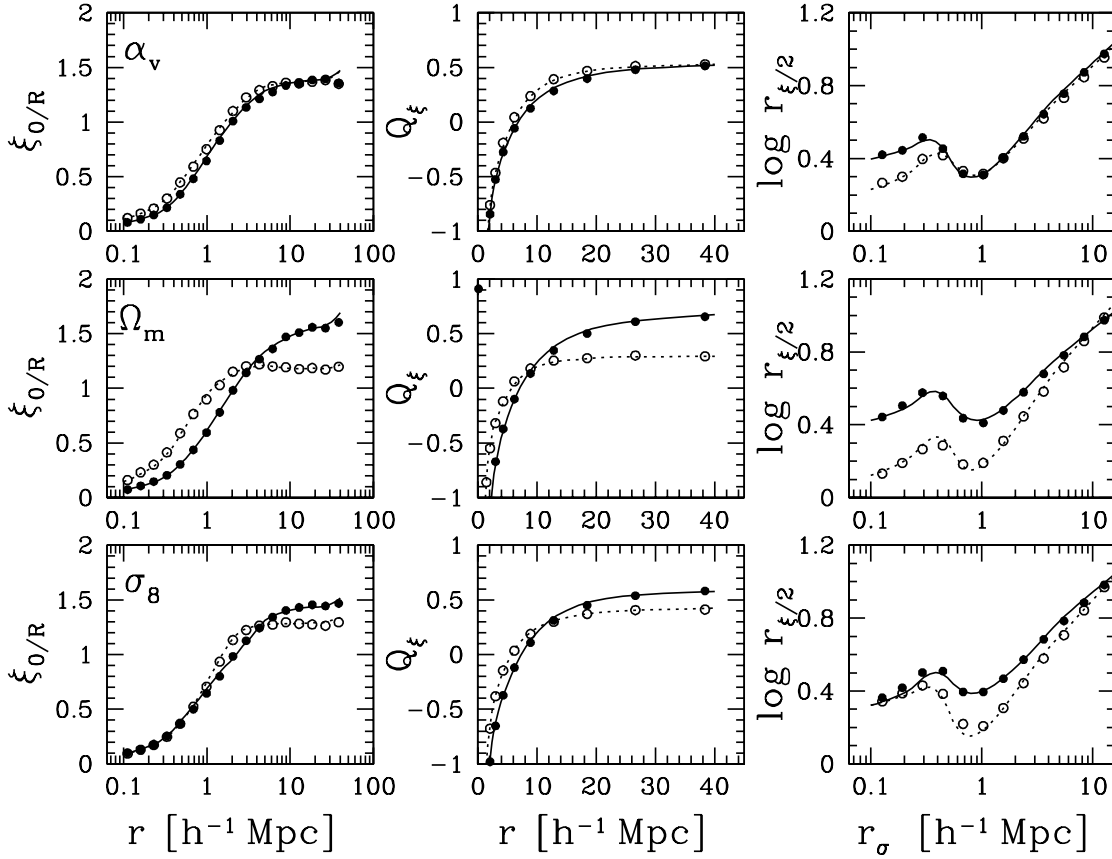


Figure 9. Measures of redshift-space clustering for various cosmologies. In each panel, the circles represent the N-body results and the lines show the model results. In each row, a cosmological parameter is varied between the high and low values used in Paper I. The top row plots results for $\alpha_v = 0.8$ (open circles; dotted lines), and $\alpha_v = 1.2$ (filled circles; solid lines). The middle row plots results for $\Omega_m = 0.1$ (open circles; dotted lines), and $\Omega_m = 0.5$ (filled circles; solid lines). The bottom row plots results for $\sigma_8 = 0.6$ (open circles; dotted lines), and $\sigma_8 = 0.95$ (filled circles; solid lines).

χ^2 per degree of freedom of the model calculation with the N-body data is approximately one.

Figures 10a and 10b plot $r_{\xi/2}$ and Q_ξ , respectively, for the input N-body data. In panel (a), the models produce degenerate $r_{\xi/2}$ values inside the one-halo term, $r_\sigma < 0.7 h^{-1}\text{Mpc}$. If α_v were set to unity for all five models, the $r_{\xi/2}$ curves would separate at small radii due to the higher velocity scale of satellite galaxies for the higher Ω_m models. Outside the one-halo term, the models separate modestly, but are distinguishable outside their errors. In panel (b), all models have the same asymptotic value of Q_ξ , but all models are below the linear theory prediction of 0.55 at all r for $\beta = 0.46$. The different values of α_v for each model cause the radii at which non-linearities set in to differ; for models with lower values of α_v , Q_ξ becomes negative at smaller r .

To explore the likelihood of cosmological parameters from these data we use the Monte Carlo Markov chain (MCMC) technique (e.g., Doran & Müller 2004). In MCMC,

a randomly chosen point in parameter space is automatically accepted as part of the chain if the χ^2 for that point is less than that of the previous point. If the χ^2 is larger, the probability of acceptance is $\exp(-\Delta\chi^2/2)$. To choose the next point in parameter space, parameters are chosen from a Gaussian distribution centered on the previously accepted point. The widths of the Gaussians are the eigenvalues of the covariance matrix of the points already in the chain. Each chain is checked for convergence using the power spectrum method of Dunkley et al. (2005). The benefit of the MCMC approach is that it allows one to marginalize over the HOD parameters; because different HODs will produce different galaxy velocity fields, it is necessary to account for uncertainties in the HOD parameters from the errors in the real-space correlation function. For each element in the chain, the total χ^2 is the sum of the χ^2 values for each of the four observables.

For this analysis we have altered the parameters of the

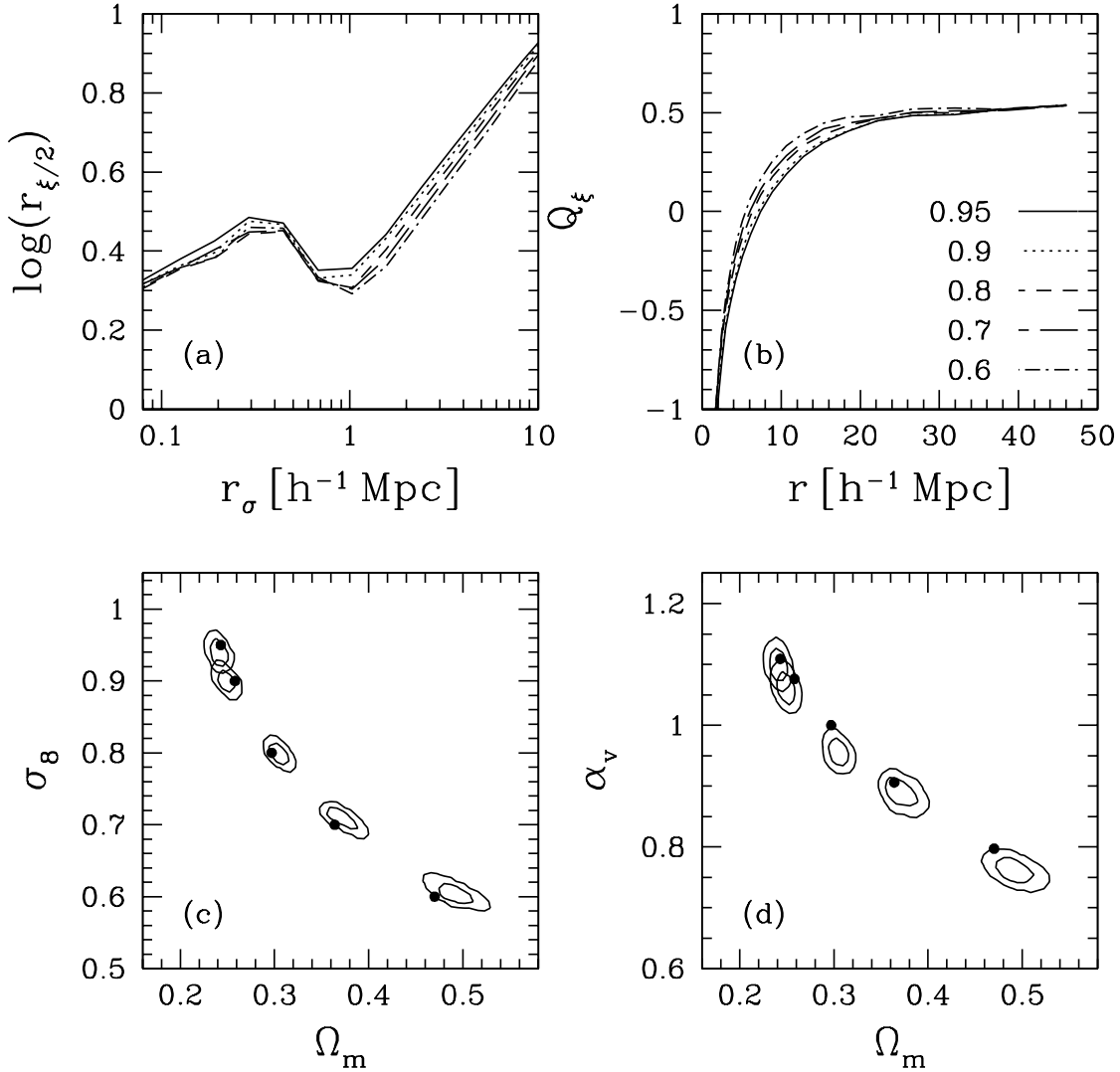


Figure 10. Recovery of input cosmological parameters from MCMC analysis for the large-scale/small-scale degenerate HOD models with the parameter values listed in Table 1. Panels (a) and (b) plot the input N-body data for two of the four observables used. Panel (a) plots $r_{\xi/2}$ as a function of r_{σ} for all five models. This quantity demonstrates the small-scale degeneracy of the models. Panel (b) plots Q_{ξ} as a function of r . This quantity demonstrates the large-scale degeneracy of the models. Panel (c) plots the 1- and 2- σ error contours in the Ω_m - σ_8 plane, marginalizing over α_v and HOD parameters. The filled circles represent the input parameters. Panel (d) shows the error contours in the Ω_m - α_v plane, marginalizing over σ_8 and HOD parameters.

Jenkins mass function to better match the mass function of our own simulations. Due to shot noise in the particle distribution, the friends-of-friends algorithm systematically overestimates the masses of halos with N less than a few hundred particles (Warren et al. 2005). At fixed (true) mass, this leads to an overestimate of the mass function by a few percent. As shown in Appendix B of Tinker et al. (2005), the slight difference between our mass function and the Jenkins fitting function creates a discrepancy between the numerical and analytic one-halo terms of $\xi_R(r)$. In the MCMC analysis, this discrepancy can drive the chain to the wrong solution even though the difference in the model results is small.

We stress that this modification is not a consequence of the model; the model will correctly describe the redshift-space distortions for any input mass function. The parameters of the Jenkins formula are (0.315, 0.61, 3.8). Our modified parameters are (0.345, 0.636, 3.43), which increases the number of halos less than M_* by $\sim 7\%$. The use of simulations with higher mass resolution would produce mass functions in better agreement with the results of Jenkins et al. (2001) and Warren et al. (2005).

Figures 10c and 10d show the constraints on the cosmological parameters from the MCMC results. Panel (c) shows the Ω_m - σ_8 projection of the parameter space, and panel (b)

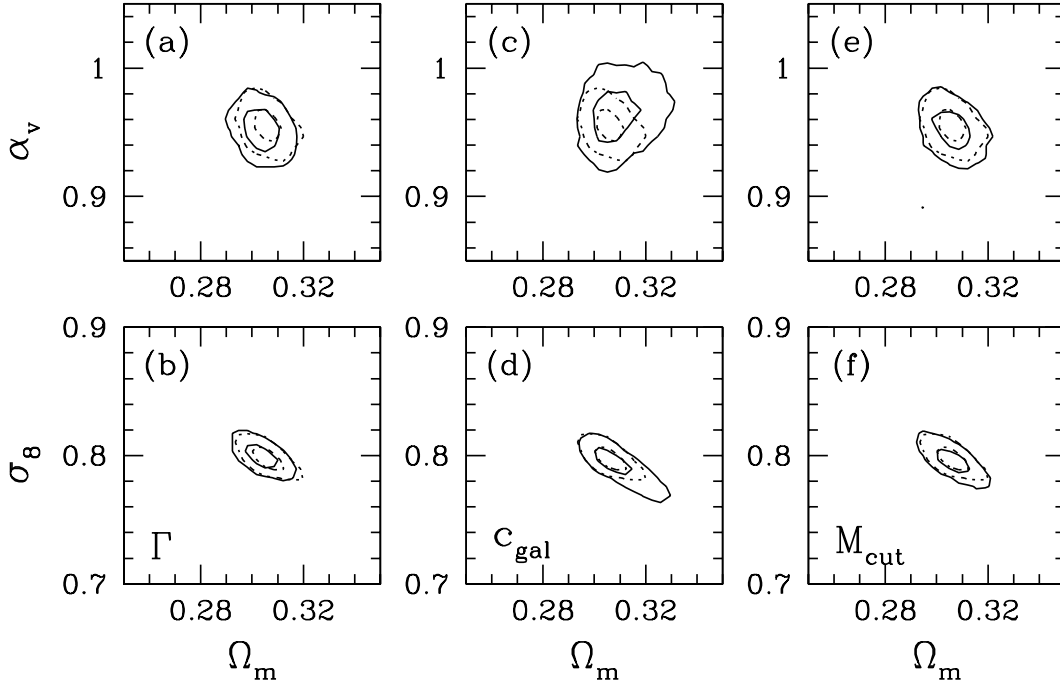


Figure 11. Constraints on Ω_m , σ_8 , and α_v for models with extra free parameters. In each panel, the dotted contours represent the error contours from Figure 10 for HOD3. The top three panels show constraints in the Ω_m - α_v plane, while the bottom panels show constraints in the Ω_m - σ_8 plane. In panels (a) and (b), the solid lines correspond to a model in which Γ is introduced as a free parameter, in addition to the HOD and cosmological parameters. In panels (c) and (d), the solid lines correspond to a model in which the ratio between the halo concentrations and the concentration parameter for satellite galaxies, $c_{\text{gal}}/c_{\text{halo}}$ is a free parameter. In panels (e) and (f), the solid lines correspond to a model in which $\langle N_{\text{sat}} \rangle_M$ contains an extra parameter M_{cut} (see equation [36]).

panel rotates the data to show the Ω_m - α_v projection. The solid circles plot the input cosmological values. The contours show the one- and two- σ confidence levels on each parameter. For most of the models listed in Table 1, the correct values are within either the one- or two- σ error contour. For the central model, the MCMC analysis correctly yields $\Omega_m = 0.306 \pm 0.006$ and $\sigma_8 = 0.799 \pm 0.009$, but the velocity bias $\alpha_v = 0.955 \pm 0.015$ is 3- σ off the true value of 1.0. For models HOD1, HOD2, and HOD4, the analytic model correctly recovers the true α_v to within 1- σ ($\sim 1.5\%$). The source of this discrepancy in HOD3 can be traced to $\xi_R(r)$; the analytic model underpredicts the amplitude of $\xi_R(r)$ for this model at $r \approx 1 h^{-1}\text{Mpc}$ (see Appendix B in Tinker et al. 2005 for a comparison between the analytic model and N-body results for this HOD). To produce a better fit to the real-space clustering, a higher value of α_{sat} is favored (1.032 versus 1.005). This increases the mean velocity dispersion of galaxies, so the likelihood is higher for a model with slightly negative velocity bias, $\sim 4.5\%$ below the true value. This discrepancy is not significant in model the other models (we will discuss the results for HOD5 presently). In tests with N-body HOD models tailored toward samples of

brighter, less abundant galaxies, this discrepancy is absent in the analytic model for $\xi_R(r)$.

Compared to HOD models 1 through 4, which recover the input cosmology to better than $\sim 2\%$ (with the exception discussed in the previous paragraph), the recovered parameters for HOD5 are barely within the 2- σ contours. The analysis yields $\Omega_m = 0.491 \pm 0.014$, $\sigma_8 = 0.607 \pm 0.010$, and $\alpha_v = 0.765 \pm 0.012$, compared with the input values of (0.47, 0.6, 0.797). The high preferred value of Ω_m drives the preferred value of α_v lower than the input value. The most likely value of σ_8 , however, is unaffected. The larger errors for this model could represent a breakdown in $\Omega_m^{0.6}$ as an approximation to the linear theory scaling of halo velocities or the inability of linear theory itself to accurately model the scaling. Further testing is required to isolate the source of the error, although it is likely outside the range of interest for the true value of Ω_m .

4.3 Adding freedom to the model

The test in the previous section made several simplifying assumptions. First, the shape of $P_{\text{lin}}(k)$ was fixed to the

true value from the simulations. Second, the radial profiles of the satellite galaxies were assumed to follow the true profiles used to populate the simulations. Third, the functional form of the HOD used in the analysis was the same as that used to create the test data.

In Figure 11, we test the robustness of the analytic model against these assumptions. Panels (a) and (b) compare the results of the MCMC analysis from Figure 10 to an analysis in which the power spectrum shape parameter Γ is added as an additional free parameter with no prior. The dotted contours represent the 1- and 2- σ constraints on the cosmological parameters from Figure 10, in which Γ is set to 0.2. The solid contours are the results once marginalized over Γ . The constraints are nearly identical, even with the added freedom to the model, and the most likely value of $\Gamma = 0.204 \pm 0.005$. As discussed in §1, altering the shape of $P_{\text{lin}}(k)$ has limited impact on the redshift-space observables employed here. But altering Γ changes the amplitude of $\xi_R(r)$ for a fixed HOD, so large deviations from the true value of Γ are easily excluded by the real-space clustering alone.

Figures 11c and 11d show the cosmological constraints of the analytic model when the galaxy density profile within halos is allowed to vary. In this model, we introduce a new parameter $a_c = c_{\text{gal}}/c_{\text{halo}}$, where c represents the concentration parameter of the NFW density profile, and c_{halo} is taken from Bullock et al. (2001). This parameter preserves the shape of the dependence of c on halo mass, but allows its normalization to vary. Panel (c) presents the constraints in the Ω_m - α_v plane from Figure 10 and from varying- a_c model. Marginalizing over a_c has a noticeable effect on the constraints. The 1- σ errors on Ω_m increase from 0.006 to 0.009, while the 1- σ errors on α_v increase from 0.015 to 0.021. Although the most likely values of Ω_m and α_v are consistent in the solid and dotted contours, marginalizing over a_c does not expand the contours in a symmetric fashion. As discussed in the previous section, the analytic model for HOD3 underpredicts $\xi_R(r)$ at $r = 1 h^{-1}\text{Mpc}$. When marginalizing over a_c , this discrepancy with $\xi_R(r)$ can be compensated for by decreasing the concentrations of the satellite galaxies, thereby shifting one-halo pairs out to larger separation. Thus, in the varying- a_c analysis, the preferred value of α_{sat} is closer to the true value of 1.005, skewing the error contours, but the constraints on α_{sat} are somewhat weaker than in the fixed- a_c analysis, yielding larger overall errors. The 1- σ constraints on a_c are 0.93 ± 0.16 . Panel (d) presents the constraints in the Ω_m - σ_8 plane for these two models. The 1- σ error contours are the same in the two models, but the extra freedom of the varying- a_c model produces a small extension of the 2- σ contour down the Ω_m - σ_8 degeneracy axis. The weaker constraints produced by the varying- a_c model are apparent in Figure 11, but they only increase the errors from $\sim 2\%$ to $\sim 3\%$ on the cosmological parameters.

Lastly, we demonstrate the robustness of the model to extra freedom in the parameterization of the HOD itself. The satellite occupation function used throughout this paper is a simple power law with two free parameters. In Figures 11e and 11f we compare the MCMC results from our

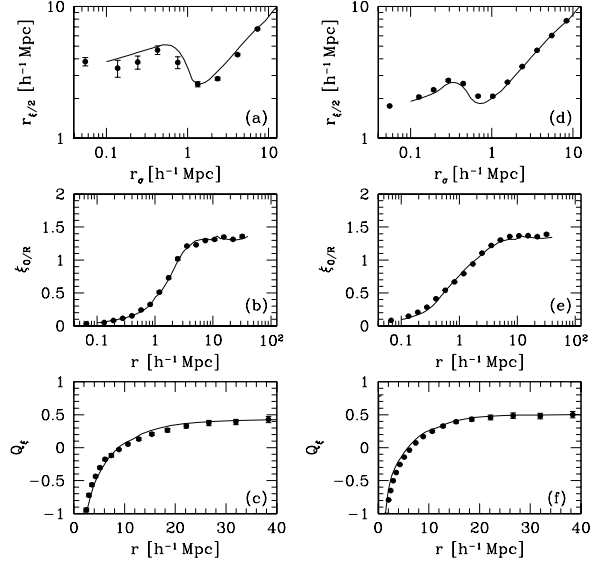


Figure 12. Left-hand panels plot the standard redshift-space observables for HOD parameters constrained to match the $M_r - 5 \log h < -21$ SDSS $w_p(r_p)$. The filled circles are N-body results for $r_{t/2}$ in panel (a), $\xi_{0/R}$ in panel (b), and Q_t in panel (c). The solid lines are the analytic model calculations for each quantity for the same HOD parameters. Right-hand panels plot the same observables, but for a model in which $\Gamma = 0.12$. The cosmology and HOD parameters are the same as HOD3 in Table 1. Points and lines are the same as panel (a)–(c).

two-parameter $\langle N_{\text{sat}} \rangle_M$ to a model with a three-parameter $\langle N_{\text{sat}} \rangle_M$ of the form

$$\langle N_{\text{sat}} \rangle_M = \left(\frac{M - M_{\text{cut}}}{M_1} \right)^{\alpha_{\text{sat}}}, \quad (36)$$

where M_{cut} is a cutoff mass scale. In equation (35), $\langle N_{\text{sat}} \rangle_M$ is cut off sharply at M_{min} . The form of equation (36) has a soft cutoff that can be at any mass, although halos below M_{min} are not allowed to host satellites. (Even with this restriction, models with $M_{\text{cut}} < M_{\text{min}}$ are not degenerate until $M_{\text{cut}} \ll M_{\text{min}}$.) However, this extra freedom in the occupation function produces a negligible effect on the cosmological constraints. Panels (e) and (f) once again compare the error contours in Ω_m - α_v and Ω_m - σ_8 planes, respectively, for the standard two-parameter $\langle N_{\text{sat}} \rangle_M$ and varying- M_{cut} model. The contours are nearly unchanged between the two models.

4.4 Other mock samples

The HOD parameters in Table 1 produce galaxy space densities consistent with the $M_r - 5 \log h < -20$ SDSS sample (Zehavi et al. 2005). Although our N-body simulations lack the resolution to model fainter samples, we can test the accuracy of the model against mock data matching to brighter samples. In Figures 12a-12c, we compare the analytic model to N-body data created with HOD parameters determined from fitting $w_p(r_p)$ measurements of the $M_r - 5 \log h < -21$ sample from Zehavi et al. (2005). To

populate the simulations, we use the HOD parameters listed in Table 3 of Zehavi et al. (2005): $M_{\min} = 5.25 \times 10^{12} h^{-1} M_{\odot}$, $M_1 = 12.3 \times 10^{14} h^{-1} M_{\odot}$, and $\alpha_{\text{sat}} = 1.39$. These HOD parameters are used to populate the simulations with $\sigma_8 = 0.9$, and the halo velocities are scaled to $\Omega_m = 0.3$. This sample yields a space density lower than the HODs in Table 1 by a factor of ~ 5 , and emphasizes higher halo masses. The N-body results are shown with the filled circles for $r_{\xi/2}$ in panel (a), for $\xi_{0/R}$ in panel (b), and Q_{ξ} in panel (c). The model calculations for the same cosmology and HOD are shown with the solid lines in each panel. For $r_{\xi/2}$, the lower space density of galaxies increases the error on this diagnostic within the one-halo term, partially from Poisson noise and partially from a less robust determination of the asymptotic value of $\xi(r_{\pi})$ at small r_{π} . But the analytic model compares favorably to the data, correctly predicting the location and depth of the minimum at $r_{\sigma} = 1.5 h^{-1} \text{Mpc}$. The analytic model also accurately predicts the shape of $\xi_{0/R}$, which has a sharper transition from linear to non-linear scales than the results in Figure 8b due to the emphasis on higher mass halos. For Q_{ξ} , the analytic model correctly describes the large-scale asymptote as well as the scale at which non-linearities set in.

In Figures 12d–12f, we compare the analytic model to N-body data created with the HOD parameters and cosmology of the central model, but populating the halos of simulations in which the shape parameter of the linear matter power spectrum is $\Gamma = 0.12$.⁴ Although a power spectrum of this shape is unable to yield acceptable HOD fits to current SDSS measurements of $w_p(r_p)$ (Z. Zheng, private communication), it is worth testing the analytic model against an extreme change in $P_{\text{lin}}(k)$. Changing the shape of $P_{\text{lin}}(k)$ alters not only the halo mass function and bias relation but the one-point distribution of dark matter densities used in the velocity model as well. For all three observables, the analytic model performs well in modeling the redshift-space clustering for a substantially different power spectrum.

This success is a strong indication that the analytic model is correctly describing the underlying physics of redshift-space distortions as it accurately describes a cosmological model quite different from the one on which it was calibrated.

5 SUMMARY

We have presented a model for the redshift-space correlation function of galaxies using the framework of the halo occupation distribution (HOD). The HOD quantifies galaxy two-point clustering by separating the total number of galaxy pairs into the contributions from within a single halo and pairs from two distinct halos. In redshift space, the one-halo term is obtained by assuming galaxies follow an isothermal, Gaussian velocity distribution with a dispersion proportional to the virial dispersion of the dark matter halo.

The constant of proportionality α_v represents the velocity bias of galaxies, and it encompasses the effects of non-isothermality, anisotropy, or systems being unrelaxed. Central galaxies are assumed to follow the center of mass of the halo they occupy. Pairs of galaxies from two distinct halos move with a combination of virial motions and the halo center of mass velocity. Halo velocity statistics have significant third and fourth moments which must be modeled to calculate redshift-space clustering. The key simplification that makes our analytic model tractable is that the pairwise distribution of halo velocities at fixed density is approximately Gaussian and approximately independent of halo mass. The non-Gaussian shape of the full distribution arises from averaging over pairs in different density environments, and the dependence of the distribution on halo mass arises because higher mass halos tend to reside in denser environments.

Our approach solves several complications in modeling pairwise velocity statistics at non-linear and quasi-linear scales. It demonstrates why halo velocity PDFs in simulations are distinctly non-Gaussian, with significant skewness and kurtosis that fluctuate with scale. The skewness arises from halo pairs in high-density environments, where pairs have high relative velocities (see also Juszkiewicz et al. 1998). The kurtosis results from a superposition of Gaussians of varying widths from halo pairs in wide-ranging environments. The model also circumvents the problem of correlated radial and tangential velocities. At a given δ , v_r and v_t are independent, and it is straightforward to calculate v_z at any angle with respect to the observer’s line of sight. The model is highly flexible in that it can describe redshift-space clustering for samples of any space density without the associated complications arising from N-body simulations that sacrifice volume for mass resolution, or resolution in favor of box size. It also eliminates the need to run large numbers of simulations when exploring parameter space.

This model can be used to obtain constraints in the $(\Omega_m, \sigma_8, \alpha_v)$ parameter space from redshift-space anisotropies following the blueprint detailed in Paper I. Observations of $w_p(r_p)$ provide tight constraints on the parameters of the HOD, separating the constraints on bias from the constraints on cosmology. Our choices for redshift-space observables largely normalize out the shapes of the real-space galaxy correlation function and the linear matter power spectrum. Marginalization over $P_{\text{lin}}(k)$ and HOD parameters do not degrade the ability of the model to constrain parameters. The only unknown quantity that notably affects these constraints is the profile of satellite galaxies within groups c_{gal} , a quantity that can be observationally measured (Yang et al. 2005) and theoretically predicted (e.g., Diemand et al. 2004; Nagai & Kravtsov 2005). Even with no prior on c_{gal} , cosmological constraints only increase by $\sim 1\%$ relative to the true value.

Our HOD approach represents a significant improvement over the dispersion model (Eq. [2]) for two main reasons. First, the HOD model circumvents the use of the redshift-space distortion parameter β entirely. The cosmological parameters Ω_m and σ_8 are direct inputs of the model, eliminating the degeneracy involved with using β to determine the matter density. Second, there are no free param-

⁴ The specifics of these simulations are identical to the $\Gamma = 0.2$ simulations. See Paper I for more discussion.

ters like σ_k , which creates a degeneracy with β as well. The velocity bias parameter α_v is a truly physical parameter that is cosmologically relevant and is a testable prediction of numerical simulations of galaxy formation and semi-analytic models. Measurements of α_v can reduce uncertainty in dynamical mass estimates of galaxy groups, utilized in group catalogs culled from large-scale optical surveys (e.g., the 2PIGG catalog of Eke et al. 2004). Alternately, studies that use the abundance of systems as a function of their velocity dispersion require knowledge of α_v to provide useful comparisons to theoretical models (Davis et al. 2005; Gerke et al. 2005). In this paper we have assumed that central galaxies are not subject to virial motions. Modest values of α_{vc} have limited effect on redshift-space clustering, but non-zero α_{vc} can easily be incorporated into the analysis of observational data and either marginalized over or constrained if the data are of sufficient precision.

Utilizing clustering information on multiple scales breaks the two primary degeneracy axes in redshift-space distortions. At large scales, linear theory correctly predicts that models with the same value of β will have the same large-scale distortions (even though linear theory is a poor descriptor of the shape of the distortions for a given value of β). This creates the degeneracy $\Omega_m^{0.6}\sigma_8 = \text{const.}$ At small scales, non-linearities are determined by the velocity scale of dark matter halos, creating the degeneracy axis $\Omega_m\alpha_v^2 = \text{const.}$ Paper I concluded that intermediate-scale clustering, $1 h^{-1}\text{Mpc} \lesssim r \lesssim 10 h^{-1}\text{Mpc}$, provides the key for breaking the large-scale/small-scale degeneracies. Here we have quantitatively demonstrated this result. The typical “banana-curve” degeneracy axes can be seen in Figures 10c and 10d, but the simulations are clearly distinguished from one another by the analytic model. The large-scale distortions set the amplitude of the $\Omega_m^{0.6}\sigma_8$ degeneracy curve, the small-scale distortions normalize the $\Omega_m\alpha_v^2$ degeneracy curve, and the intermediate-scale clustering locates the model along both curves.

The current data releases of the SDSS and 2dFGRS have reached the necessary volume and statistics to implement this HOD analysis. The ability to extract information from galaxy clustering measurements at quasi-linear and non-linear scales enables precise constraints on our specified subset of cosmological parameters that can be competitive with large-scale measures such as CMB anisotropies, Lyman- α forest, and the large-scale galaxy power spectrum. Although constructed on more fundamental physics, these methods are sensitive to quantities like the CMB tensor-to-scalar ratio, mass of the neutrino, and curvature of the inflationary fluctuation spectrum. For small-scale galaxy clustering, modest changes in the shape of $P_{\text{in}}(k)$ have marginal impact on halo occupation constraints. Thus redshift-space clustering measurements provide a powerful and complementary method for estimating the amplitude of dark matter clustering and the mean matter density of the universe.

I would like to thank Andreas Berlind, Juna Kollmeier, Andrey Kravtsov, Roman Scoccimarro, Jaaiyul Yoo, Andrew

Zentner, and Zheng Zheng for useful discussions, and Volker Springel for providing the public GADGET code. I would especially like to thank David Weinberg for his help with many aspects of this paper. The simulations were performed on the Beowulf and Itanium clusters at the Ohio Supercomputing Center under grants PAS0825 and PAS0023. I acknowledge the support of a Distinguished University Fellowship at the Ohio State University during the course of this work. This work was also supported by NSF grants AST-0098584 and AST-0407125.

APPENDIX A: OUTLINE OF TWO-HALO TERM

For the convenience of readers who wish to implement our model, we present a concise outline of the calculation of $\xi_{2h}(r_\sigma, r_\pi)$, beginning with the definition of the streaming model,

$$1 + \xi_{2h}(r_\sigma, r_\pi) = \int_{-\infty}^{\infty} [1 + \xi_{2h}^R(r)] P_{2h}(v_z|r, \phi) dv_z, \quad (\text{A1})$$

where $r^2 = r_\sigma^2 + z^2$, $v_z = H(r_\pi - z)$, and $\cos \phi = r_\sigma/r$. $\xi_{2h}^R(r)$ is the two-halo contribution to the real-space correlation function, and $P_{2h}(v_z|r, \phi)$ is the line-of-sight velocity PDF of galaxy pairs from two distinct halos. The velocity PDF in equation (A1) is a pair-weighted average over all possible combinations of halo masses. For a given halo pair, M_1 and M_2 , the line-of-sight PDF is an integral over all possible densities in which that pair can exist.

The line-of-sight PDF of a halo pair at density δ is

$$P_{g+h}(v_z|\phi, r, M_1, M_2, \delta) = \sum_{i=1}^4 \frac{w_i}{\sqrt{2\pi}\sigma_i} \exp\left[-\frac{(v_z - \mu_r \sin \phi)^2}{2\sigma_i^2}\right], \quad (\text{A2})$$

where each term in the summation represents a different combination of central and satellite galaxy pairs from the two halos. The dispersion for each term is

$$\sigma_i^2 = (\sigma_t^2 \cos^2 \phi + \sigma_r^2 \sin^2 \phi) + [\sigma_{\text{gal}}^{(i)}]^2, \quad (\text{A3})$$

where σ_t and σ_r are the tangential and radial dispersions of the dark matter halos, and $\sigma_{\text{gal}}^{(i)}$ is the dispersion of the galaxy pair from internal halo motions, defined by equation (4). The radial dispersion is

$$\sigma_r = 200 \left(\frac{\Omega_m}{0.3}\right)^{0.6} \left(\frac{\sigma_8}{0.8}\right) \left(\frac{\tilde{\rho}}{\tilde{\rho}_{200,r}}\right)^\alpha \text{ km s}^{-1}, \quad (\text{A4})$$

where

$$\tilde{\rho}_{200,r}(M_1, M_2, r) = \left(\frac{r}{5.0R_{\text{vir},1}^{1/2}}\right)^{-4.0} + \left(\frac{r}{11.5R_{\text{vir},0}^{1/2}}\right)^{-1.3} + 0.50, \quad (\text{A5})$$

and

$$\alpha(r) = \left(\frac{r}{35h^{-1}\text{Mpc}}\right)^{0.1}. \quad (\text{A6})$$

For the tangential velocities, $\tilde{\rho}_{200,r}$ is replaced in equation (A4) with

$$\tilde{\rho}_{200,t}(M_1, M_2, r) = \left(\frac{r}{7.2R_{\text{vir},1}^{1/2}} \right)^{-2.5} + \left(\frac{r}{12.6R_{\text{vir},0}^{1/2}} \right)^{-0.8} + 0.48. \quad (\text{A7})$$

The units of r and R_{vir} are $h^{-1}\text{Mpc}$. The mean velocity μ of equation (A2) is given by the spherical collapse model (eq. [18]) at $r \leq 4 h^{-1}\text{Mpc}$, linear theory (eq. [15]) at $r \geq 20 h^{-1}\text{Mpc}$, and a linear combination of the two at intermediate scales,

$$\mu(r, \delta) = w \mu_{\text{sc}} + (1 - w) \mu_{\text{lin}}, \quad (\text{A8})$$

with

$$w = \begin{cases} 1 & \text{if } r \leq 4 \\ 1.86 - 0.62 \ln r & \text{if } 4 \leq r < 20 \\ 0 & \text{if } r < 20. \end{cases} \quad (\text{A9})$$

The distribution function $P_{g+h}(v_z|r, \phi, M_1, M_2, \delta)$ is integrated over all δ to obtain

$$P_{g+h}(v_z|\phi, r, M_1, M_2) = \int_{-1}^{\infty} P_{g+h}(v_z|\phi, r, M_1, M_2, \delta) P_m(\delta|r, M_1, M_2) d\delta, \quad (\text{A10})$$

where the PDF of dark matter density used in equation (A10) is given by

$$P_m(\delta|r, M_1, M_2) = A \exp \left[\frac{1.45(b_1 + b_2) + (r/9.4R_{\text{vir},1})^{-2.2}}{1 + \delta} \right] P_m(\delta|r) \quad (\text{A11})$$

and

$$P_m(\delta|r) = \frac{1}{2\pi\sigma_1^2} \exp \left[-\frac{[\ln(1 + \delta) + \sigma_1^2/2]^2}{2\sigma_1^2} \right] \frac{1}{1 + \delta}, \quad (\text{A12})$$

where $\sigma_1^2(r) = \ln[1 + \sigma_m^2(r)]$ and $\sigma_m(r)$ is the mass variance in top-hat spheres of radius r . To calculate $\sigma_m(r)$, we use the non-linear matter power spectrum of Smith et al. (2003) to better describe the distribution of dark matter at small scales. To calculate the halo bias factors, we use the function in Appendix A of Tinker et al. (2005). The final step is to integrate over all halo pairs,

$$P_{2h}(v_z|r, \phi) = 2(\bar{n}'_g)^{-2} \int_0^{M_{\text{lim},1}} dM_1 \frac{dn}{dM_1} \langle N \rangle_{M_1} \int_0^{M_{\text{lim},2}} dM_2 \frac{dn}{dM_2} \langle N \rangle_{M_2} P_{g+h}(v_z|r, \phi, M_1, M_2), \quad (\text{A13})$$

where \bar{n}'_g is given by equation (9), and the limits of the integral are determined by the condition that no halo pair can be closer than the sum of their virial radii. Using the relation $R_{\text{vir}} = (3M/4\pi\bar{\rho}\Delta_{\text{vir}})^{1/3}$ (recall that we have defined $\Delta_{\text{vir}} = 200$ throughout this paper),

$$\begin{aligned} M_{\text{lim},1}(r) &= r - R_{\text{vir}}(M_{\text{min}}) \\ M_{\text{lim},2}(r) &= r - R_{\text{vir}}(M_1). \end{aligned} \quad (\text{A14})$$

Equation (A13) is inserted directly into equation (A1).

REFERENCES

- Abazajian, K., et al. ApJ (submitted), astro-ph/0408003
 Bean, A. J., Ellis, R. S., Shanks, T., Efstathiou, G., & Peterson, B. A. 1983, MNRAS, 205, 605
 Benson, A. J. 2001, MNRAS, 325, 1039
 Berlind, A. A., & Weinberg, D. H. 2002, ApJ, 575, 587
 Berlind, A. A., Weinberg, D. H., Benson, A. J., Baugh, C. M., Cole, S., Davé, R., Frenk, C. S., Katz, A., & Lacey, C. G. 2003, ApJ, 593, 1
 Bond, J. R., Cole, S., Efstathiou, G., & Kaiser, N. 1991, ApJ, 379, 440
 Bullock, J. S., Kolatt, T. S., Sigad, Y., Somerville, R. S., Klypin, A. A., Primack, J. R., Dekel, A. 2001, MNRAS, 321, 559
 Cole, S., Fisher, K. B., & Weinberg, D. H. 1994, MNRAS, 267, 785
 Cole, S., Fisher, K. B., & Weinberg, D. H. 1995, MNRAS, 275, 575
 Coles, P., & Jones, B. 1991, MNRAS, 248, 1
 Colless, M. et. al. 2001, MNRAS, 328, 1039
 Collister, A. A., & Lahav, O. 2004, MNRAS (submitted), astro-ph/0412516
 Cooray, A. & Sheth, R. K. 2002, Phys. Rep., 372, 1
 Cooray, A., 2004, MNRAS, 348, 250
 Davis, M. & Peebles, P. J. E. 1983, ApJ, 267, 465
 Davis, M., Efstathiou, G., Frenk, C. S., & White, S. D. M. 1985, ApJ, 292, 371
 Davis, M., Gerke, B. F., & Newman, J. A. 2005, ASP Conference 339: Observing Dark Energy, (astro-ph/0408344)
 Diemand, J., Moore, B., & Stadel, J. 2004, MNRAS, 352, 535
 Doran, M. & Müller C. M. 2004, JCAP, 409, 3
 Dunkley, J., Bucher, M., Ferreira, P. G., Moodley, K., & Skordis, C. 2005, MNRAS, 356, 925
 Efstathiou, G., Bond, J. R., & White, S. D. M. 1992, MNRAS, 258, 1
 Eke, V. R., et al. 2004, MNRAS, 348, 866
 Faltenbacher, A., Kravtsov, A. V., Nagai, D., & Gottlöber, S. 2004, MNRAS (submitted), astro-ph/0408488
 Fisher, K. B., Davis, M., Strauss, M. A., Yahil, A., & Huchra, J. P. 1994, MNRAS, 267, 927
 Fisher, K. B. 1995, ApJ, 448, 494
 Fisher, K. B. & Nusser, A. 1996, MNRAS, 279, L1
 Gerke, B. F. et al. 2005, ApJ, 625, 6
 Ghigna, S., Moore, B., Governato, F., Lake, G., Quinn, T., & Stadel J. 2000, ApJ, 544, 616
 Hamana, T., Issha, K., Yoshida, N., Suto, Y., & Jing, Y. P. 2003 MNRAS, 343 1312
 Hatton, S. & Cole, S. 1999, MNRAS, 310, 1137
 Hawkins, E., Maddox, S., Cole, S., et al. 2003, MNRAS, 346, 78
 Jenkins, A., Frenk, C. S., White, S. D. M., Colberg, J. M.,

- Cole, S., Evrard, A. E., Couchman, H. M. P., & Yoshida, N. 2001, MNRAS, 321, 372
- Jing, Y. P., Mo, H. J., & Boerner, G. 1998, ApJ, 494, 1
- Juszkiewicz, R., Fisher, K. B., Szapudi, I. 1998, ApJ, 504, L1
- Juszkiewicz, R., Springel, V., Durrer, R. 1999, ApJ, 518, L25
- Kaiser, N. 1987, MNRAS, 227, 1
- Kang, X., Jing, Y. P., Mo, H. J., & Börner, G. 2002 MNRAS, 336, 892
- Klypin, A., Gottlöber, S., Kravtsov, A. V., and Kohklov, A. M. 1999, ApJ, 516, 530
- Kofman, L., Bertschinger, E., Gelb, J. M., Nusser, A., & Dekel, A. 1994, ApJ, 420, 44
- Kravtsov, A. V., Berlind, A. A., Wechsler, R. H., Klypin, A. A., Gottlöber, S., Allgood, B., Primack, J. R. 2004, ApJ, 609, 35
- Lin, Y.-T., Mohr, J. J., & Stanford, S. A. 2004, ApJ, 610, 745
- Mo, H. J., & White, S. D. M. 1996, MNRAS, 282, 1096
- Ma, C. & Fry, J. N. 2000, ApJ, 543, 503
- Madgwick, D. S., et al. 2003, MNRAS, 344, 874
- Nagai, D. & Kravtsov, A. V. 2005, ApJ, 618, 557
- Park, C., Vogeley, M. S., Geller, M. J., & Huchra, J. P. 1994, ApJ, 431, 569
- Pavlidou, V. & Fields, B. D. 2005, PhysRevD, 71, 043510
- Peacock, J. A. & Dodds, S. 1994, MNRAS, 267, 1020
- Peacock, J. A., Smith, R. E. 2000, MNRAS, 318, 1144
- Peacock, J. 1999, *Cosmological Physics*, Cambridge University Press
- Peebles, P. J. E. 1976, ApJ, 205, L109
- Peebles, P. J. E. 1979, AJ, 84, 730
- Peebles, P. J. E. 1980, *The Large-Scale Structure of the Universe*
- Percival, W. J. et al. 2002, MNRAS, 337, 1068
- Sargent, W. L. W. & Turner, E. L. 1977, ApJ, 212 L3
- Scoccimarro, R., Sheth, R. K., Hui, L., & Jain, B. 2001, ApJ, 546, 20
- Scoccimarro, R. 2004, PhysRevD, 70, 063001
- Seljak, U. 2000, MNRAS, 318, 203
- Seljak, U. 2001, MNRAS, 325, 1359
- Sheth, R. K. 1996, MNRAS, 279, 1310
- Sheth, R. K. & Tormen, G. 1999, MNRAS, 308, 119
- Sheth, R. K. & Diaferio, A. 2001, MNRAS, 322, 901
- Sheth, R. K., Hui, L., Diaferio, A., & Scoccimarro, R. 2001a, MNRAS, 325, 1288
- Sheth, R. K., Diaferio, A., Hui, L., & Scoccimarro, R. 2001b, MNRAS, 326, 463
- Sheth, R. K. & Tormen, G. 2002, MNRAS, 329, 61
- Skibba, R., Sheth, R. K., Connolly, A. J., & Scranton, R. 2005, MNRAS (submitted), astro-ph/0512463
- Slosar, A., Seljak, U., & Tasitsiomi, A. 2006, MNRAS, 366, 1455
- Smith R. E., et al. 2003, MNRAS, 341, 1311
- Spergel, D. N., et. al. 2003, ApJ, 148, 175
- Springel, V., Yoshida, N., & White, S. D. M. 2001 NewA, 6, 79
- Tegmark, M., et. al. 2004a, ApJ, 606, 702
- Tegmark, M., et. al. 2004b, PhysRevD, 69, 103501
- Tinker, J. L., Weinberg, D. H., Zheng, Z., & Zehavi, I. 2005, ApJ, 631, 41 astro-ph/0411777
- Tinker, J. L., Weinberg, D. H., & Zheng, Z., I. 2006a, MNRAS (accepted), astro-ph/0501029
- Tinker, J. L., Norberg, P., Weinberg, D. H., & Warren, M. S. 2006b, ApJ (submitted), astro-ph/0603543
- van den Bosch, F. C., Weinmann, S. M., Yang, X., Mo, H. J., Li, C., & Jing, Y. P., 2005, MNRAS (submitted), astro-ph/0502466)
- Warren, M. S., Abazajian, K., Holz, D. E., & Teodoro, L. 2005, ApJL, submitted, (astro-ph/0506395)
- White, M. 2001, MNRAS, 321, 1
- Yang, X., Mo, H. J., & van den Bosch, F. C. 2003, MNRAS, 339, 1057
- Yang, X., Mo, H. J., Jing, Y. P., van den Bosch, F. C., & Chu, X. Q. 2004, MNRAS, 350, 1153
- Yang, X., Mo, H. J., van den Bosch, F. C., Weinmann, S. M., Li, C., & Jing, Y. P. 2005, MNRAS, submitted, (astro-ph/0504477)
- York, D., et al. 2000, AJ, 120, 1579
- Yoshikawa, K., Jing, Y. P., & Börner, G. 2003, ApJ, 590, 654
- Zehavi, I., Weinberg, D. H., Zheng, Z., Berlind, A. A., Friedman, J. A., et al. 2004, ApJ, 608, 16
- Zehavi, I., et al. 2005, ApJ, 630, 1
- Zheng, Z. 2004, ApJ, 610, 61
- Zheng, Z., Tinker, J. L., Weinberg, D. H., & Berlind, A. A. 2002, ApJ, 575, 617
- Zheng, Z., Berlind, A. A., Weinberg, D. H., Benson, A. J., Baugh, C. M., Cole, S., Davé, R., Frenk, C. S., Katz, A., & Lacey, C. G. 2005, ApJ, 633, 791
- Zurek, W. H., Quinn, P. J., Salmon, J. K., & Warren, M. S. 1994, ApJ, 431, 559